

What does Finite Volume-based implicit filtering really resolve in Large-Eddy Simulations?

Filippo Maria Denaro *

Dipartimento di Ingegneria Aerospaziale e Meccanica, Seconda Università di Napoli, via Roma 29, 81031 Aversa, Italy
Institute for High-Performance Computing and Networking (ICAR), CNR, via Pietro Castellino 111, I-80131 Naples, Italy

ARTICLE INFO

Article history:

Received 20 August 2010

Received in revised form 8 February 2011

Accepted 9 February 2011

Available online 16 February 2011

Keywords:

Large-Eddy Simulation

Integral conservation laws

Finite Volume methods

Implicit filtering

Modified wavenumber analysis

ABSTRACT

The study illustrated in this paper completes the topics initially investigated in Ref. [42], the aim being here to analyze the role of the integral-based Finite Volume (FV) discretizations in Large Eddy Simulations that exploit the implicit filtering approach. Specifically, a theoretical study on the effective shape and length of three-dimensional filters induced by some FV-based flux reconstructions is the object of this paper. For any integral-based flux reconstruction, one gets always an approximation of the top-hat filter kernel. This is not the case of the filters induced by the differential-based Finite Difference operators, such as those reported and analyzed in Refs. [16,24]. Considering the sub-filter resolution parameter $Q = \Delta_{\text{eff}}/h$, being Δ_{eff} the effective filter width and h the computational grid size, allows us discerning the effective measure of the approximate built-in top-hat filter. The induced shape and width is analyzed by means of a *modified wavenumber-like* analysis that is developed in the 3D Fourier space. Several evaluation criteria applied on different schemes are considered and the differences in terms of either velocity or flux interpolations on staggered or non-staggered grids are analyzed. Conclusions are reported that, depending on the using of either the integral or the differential form of the filtered equations, the induced numerical filter is or is not a congruent approximation of the exact top-hat transfer function for some value Q . The need of a suitable estimation of the sub-filter parameter Q is assessed from several real LES computations, that make use of the new integral-based version of the eddy-viscosity dynamic modeling presented in Ref. [42]. In fact, it is shown that the test-filtering length has to be carefully chosen as a function of the FV-based induced filter.

© 2011 Elsevier Inc. All rights reserved.

1. Introduction

Large Eddy Simulation (LES) of turbulence aims to reduce the degree of freedom of the flow problem by separating large (resolved) and Sub-Grid Scales (SGS, unresolved) of the fluid motion. In principle, this goal is obtained by applying a low-pass filtering operator on the point-wise governing equations. Nevertheless, such filtering operation is often nothing but formalism in writing the continuous form of the LES equations. Indeed, in the so-called *implicit filtering approach* to LES, the discretization of both domain and differential operators is used in practice as built-in filtering, see Refs. [1–4]. Since a numerical representation of the filtered variables is associated with a finite number of resolved scales and marginal resolution, any discrete model can induce significant alterations in the resolved scales' dynamic. The implicit filtering technique is to date the

* Address: Institute for High-Performance Computing and Networking (ICAR), CNR, via Pietro Castellino 111, I-80131 Naples, Italy. Fax: +39 081 5010264.
E-mail address: denaro@unina.it

most widely used approach in LES although, in order to identify unambiguously the filter type, the suitability of using the explicit filtering technique (pre-filtering) has been analyzed [5–9,51].

This paper analyses the implicit filters resulting from the adoption of the integral-based LES equations, discretized in a Finite Volume (FV) manner, since such discretization is feasible for engineering problems, e.g. see Ref. [10]. According to Refs. [11,12], three different levels of approximation exist for FV-based methods: interpolation, differentiation and integration. Using the integral form rather than the differential form (used for Spectral Methods (SM) and Finite Difference (FD) methods) appears, therefore, significantly more complicated. However, the FV approach solves discrete equation models that allow us to conserve *a priori* the resolved quantity, regardless of the actual accuracy order of the method, e.g. see Ref. [40]. This is an advantage over SM and FD methods, which do not automatically ensure such property. The discrete conservation property ensures the correct wave velocity propagation of high flow gradient components as it is required to reproduce the correct energy dynamic [11].

Historically, the introduction of the FV methods for LES goes back as far as the original simulations of Smagorinsky (1963), subsequently formalized by Arakawa (1963), Lilly (1965) and Bryan (1966), and taken up by Deardorff (1970) and Schumann (1975) in early LES studies [1–4]. FV methods somehow fell into disfavor as the spectral approach of Orszag (1971) was viewed as more accurate for fundamental studies. Nevertheless, FV-based methods have continued to be used to date and are currently returning to favor as a flexible and economic means of simulating flows in complex industrial and environmental problems. Nowadays, both commercial and open-source codes are based on FV methods and are supplied with modern SGS modeling (e.g. the dynamic Smagorinsky modeling) while exploiting the built-in FV-based filtering procedure.

In actual fact, since the beginning of such historical studies, the discretization of the filtered equation written in divergence form was denoted the “FV method”, a term used ambiguously to date, e.g. see Refs. [16,24]. Conversely, in accord with a well-established literature (see Refs. [11,12]), the “FV method” is referred to here as a discretization of the integral conservation laws¹ (see also Refs. [13–15,40]). Accordingly, any type of numerical flux reconstruction always drive to update the discrete cell-variable that results in a unique approximation² of the *top-hat* filtered variable (which is a smooth filtering in wavenumber space [27]), associated with the local volume average over a small domain of linear measure Δ , e.g. see Refs. [13–15].

Furthermore, the discretization of the computational domain introduces the characteristic grid length h , which implies the action of the additional projective grid-filtering acting at the Nyquist cut-off frequency π/h . In LES practice, h is an input length to be prescribed whereas the filter length Δ is not prescribed but implicitly depends upon the type of numerical method by means of the *sub-filter resolution* parameter $Q = \Delta/h$ [1,16,18,24,25]. Only for sufficiently high values of Q the relevance of the marginal numerical resolution could be disregarded [45]. In fact, $Q = 1$ –2 typically results in implicit FV-based filtering LES and closure modeling also contains important contributions which are sensitive to the adopted spatial discretization [24]. Thus, discretizations of the filtered equations and the resulting numerical errors (local truncation error, aliasing) have been analyzed in many papers [8,13,15,16,18,20–25,28], although the conclusions drawn are not always consistent. The relevance of using FV-based LES equations has been marginally highlighted in recently published papers, e.g. see Refs. [7,16], but referring to as explicit filtering formulations applied on the differential governing LES equations [5–9,51].

One of the main conflicting issues to be addressed concerns the fact that FV and FD discretizations are often considered formally equivalent, especially on equidistant meshes, the difference being simply supposed to be an invertible matrix. Considering an averaged value stored in the cells is sometimes thought to be unnecessary, the *top-hat* filter is merely considered as a construct, which is added to the formulation if an FV discretization is selected. Consequently, the type of FV-based transfer function could be inferred from the FD-based one, e.g. see Ref. [24]. Hence, an FV formulation is thought to be affected by the same ambiguities in its discretization and its inferred implicit filter as an FD approach. These opinions can be explained by the fact that central second order FD methods have been selected, for many years, as implicit applications of *top-hat* filtering, creating confusion in the true distinction between FD and FV methods in the LES field [12].

It is the authors' opinion that, according to the integral conservation laws, the governing equations in “genuine” FV discretizations have to be integrated over cell-volumes, enabling us to solve for discrete variables (stored in the cell centers) that *must* be an approximation of the cell-averaged (*top-hat* filtered) variable. An initial look at the classic CFD analysis on FV and FD methods reveals some key foundations. For instance, Ferziger and Peric's book [12], introduces the chapter on the FV method with (page 71): “... uses the integral form of the conservation equation as the starting point” and the “algebraic equation for a particular FV is obtained when the surface and volume integrals are approximated using quadrature formulae”. Moreover, it is clearly stated (page 72) that “depending on the approximations used, the resulting (discrete) equations may or may not be those obtained from the FD method”. Moreover, Leveque [11] provides a framework for understanding the relationship between the integral conservation laws and the “weak form” that is a

¹ It is worthwhile remarking that, since FV methods can be rewritten as particular cases of the variational Galerkin method, i.e. a projection along suitable shape functions, the Finite Element approach is also a possible candidate for implicit filtering weak form-based LES, e.g. see Refs. [38,49]. Furthermore, FV approaches are also cited in the framework of implicit sub-grid modeling (ILES), see Ref. [39], providing us with some insights into the FV-based induced LES filter.

² Deconvolution procedures, which would be able to change the spectral resolution, are not considered in this study.

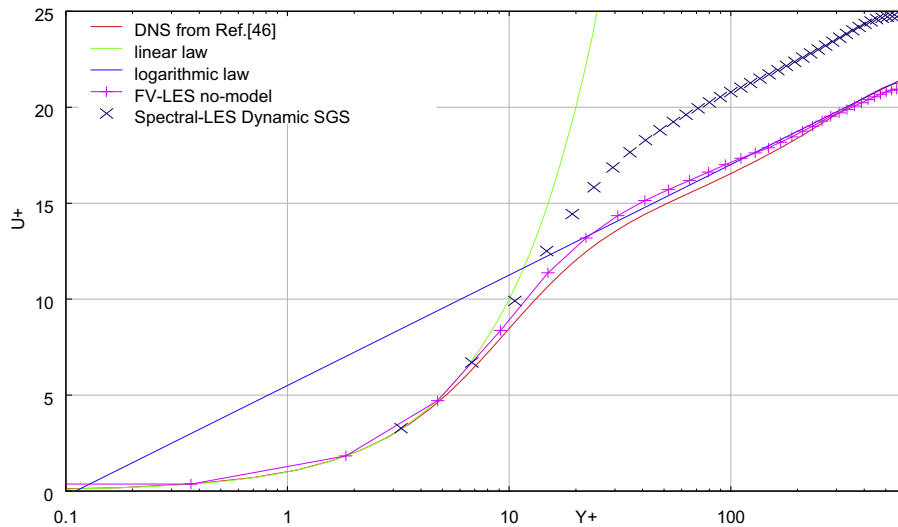


Fig. 1a. Statistically averaged stream-wise velocity profiles of turbulent channel flow at $Re_\tau = 590$ for FV-based LES no-model versus Spectral-based LES with dynamic SGS modeling. DNS data are taken from Ref. [46].

modified differential equation governing the solution of averaged values (page 64). As opposed to point-wise approximations at grid points, which are typical of FD methods, the total integral of a variable is approximated over each FV (page 5): “These values are modified in each time step by the flux through the edges of the FV, and the primary problem is to determine good numerical flux functions that approximate the correct fluxes reasonably well, based on the approximate cell averages, the only data available”. Note that assuming *cell-averaged value* = *cell-center value* is a second order accurate numerical approximation, higher order flux reconstructions being possible [11,12] in FV methods and requiring a high degree of accuracy in both interpolation and integration formulas. Actually, the use of high order flux reconstruction does not imply a change of the volume-averaged variable (unless deconvolution procedure are introduced, see Ref. [13,14,34]) governed by the integral conservation law. Conversely, FD methods induce as different filtered variables as the accuracy order of the discrete derivative is increased, tending towards the spectral cut-off filter for (hypothetical) infinite accuracy order, see Refs. [13,14,16,24]. When analyzing the divergence and the integral-based form in LES framework, it is worthwhile highlighting the differing decomposition in resolved and unresolved fluxes. Indeed, the commutative property between filter and divergence operators must be invoked while using the divergence form but this is no longer necessary using the integral-based form. A new integral-based SGS dynamic procedure has been introduced consequently, which enables the Germano identity to be properly rewritten, and the multi-dimensional character of the model constant to be preserved, see Refs. [14,15,17,42].

In order to focus more closely on the aims of this study, it is instructive to initially show an example of numerical solutions obtained for the problem of the turbulent channel flow [46] at $Re_\tau = 590$. An FV-based second order accurate [17,26,42] code was run without using any turbulence modeling, on a $64 \times 64 \times 80$ computational grid (details are reported in the results section), sufficiently coarse to ensure that we had in fact a no-model LES. Being the unresolved terms simply disregarded, only the smoothing implicitly induced by the FV method is present, therefore such a simulation is expected to produce a clear wrong solution. In order to provide a correct comparison with a real LES, the solution obtained on a $64 \times 80 \times 64$ grid with an SM-based code [42] supplied by a dynamic eddy viscosity model, was considered.³ The statistically averaged stream-wise velocity profiles, together with the DNS result [46], are shown in Fig. 1a. Despite neglecting the SGS contribution, the FV-based solution is stable, it shows only a slight deviation from the logarithmic slope but appears better than that of the SM, which overestimates the DNS profile. It is well known that, even using spectral methods, eddy viscosity SGS models can induce an overestimation of the logarithmic region (see Refs. [42,44,45,47,50]). Of course, one may check for higher order statistics, for example energy spectra, to figure out which is the best solution. For the sake of brevity, other plots are not reported (for details see Ref. [42]) but FV and SM energy spectra showed a relatively similar smoothing of the highest resolved wavenumbers.

Thus, these solutions make us wonder what the SGS model would really do to further improve the FV-based no-model result. In fact, if an eddy viscosity model was added to the no-model FV-based filtered equations it is plausible to conjecture an overestimation of the resulting velocity profile. Hence, one question can be formulated: *should the DNS profile be considered as a correct comparison term of LES solutions for any type of implicit filter and, consequently, should any overestimation of the*

³ The spectral LES code was originally developed by Zikanov et al., see Ref. [41], and the code was slightly modified to solve the channel flow in some tests performed with my colleague De Stefano. No modifications have been made on the original SGS modeling. We thank the authors for kindly providing the code.

DNS profile be considered a mere error produced by the eddy viscosity modeling⁴ or must the overestimation be accepted in some degree as correct behavior due to the action of a certain type of implicit filter?

It is the author's opinion that, even in a hypothetical absence of any numerical and modeling approximations, the “ideal” integral-based LES solution would not be exactly comparable to DNS, owing to both the finite representation and the smoothing of resolved frequencies induced by the shape of the implicit filter. Thus, in order to have a more meaningful comparison, a suitable post-filtered DNS solution, where an explicit filter mimics the built-in filtering of the integral formulation, should be used. As a matter of fact, it is well known that the use of post-filtered DNS solutions is not fully consistent for an analysis of the quality of LES solutions since these latter solutions adapt themselves during the real computation [1–4]. The effective role of the built-in filter should be highlighted directly from the analysis of the FV-based numerical approximation since the smoothing induced by the transfer function must be taken into account to understand the quality of the LES solution.

The paper is organized as follows: Sections 2 and 3 illustrate the framework of the integral governing equation and its FV-based discretization and clarify the aspect of the implicit filtering inherent to an FV method and to the computational grid. A comparison with FD-based LES equations is also illustrated. Then, in order to detect the filter shape induced by an FV method, in analogy with the *modified wavenumber* analysis, the 3D numerical transfer functions in effects for each *numerical non-linear flux function* are deduced and compared to the exact one. Several FV formulae of second and higher order are analyzed, both for non-staggered and staggered centered collocation of the velocity components. Once deduced the exact FV-based transfer function, its effective width is parameterized by the sub-filter parameter, that is $\Delta_{eff} = Qh$, and is then compared to the numerical ones, to attempt to find some value of the parameter Q to minimize the error. This approach appears distinctive from those performed by other authors, see Refs. [18,24,25], which analyze the combined filtering effects by considering the role of the local truncation error in the *modified differential equation*. Unlike Ref. [24], here we also present the full multidimensional FV discretizations analyzed in the Fourier space while taking into account the non-linear product of the wavenumber components. A key-discussion in Section 3.4 focuses on FD and FV methods while distinguishing the discretization of the differential divergence form and the integral form in terms of the top-hat filter. Finally, Section 4 illustrates a group of real LES computations on turbulent flows. The new integral-based FV version of the dynamic procedure is presented [42], illustrating the natural remedy to the mathematical inconsistency of the extraction of the modeling coefficient out of filtering. Two eddy viscosity models were tested, both highlighting the relevance of the numerical filter parameters on the computed statistics.

2. Integral versus differential-based filtered formulations in continuous form: the flux decomposition

In the LES approach, as has been recognized since [19] the mid-70s, scale separation is obtained via low-pass filtering. The spatial filtering operation (no time-filtering is considered here) can be expressed as the convolution product between an unfiltered point-wise field, say ϕ , and some suitable filter function G , that is

$$\bar{\phi}(\mathbf{x}, t; \Delta) = \int_{R^3} G(\mathbf{x} - \mathbf{x}'; \Delta) \phi(\mathbf{x}', t) d\mathbf{x}' \equiv G * \phi. \quad (1)$$

Δ being the characteristic filter width that can be expressed in terms of some norm on the multidimensional width vector. Some classic LES filters G are the top-hat in physical space, the sharp spectral cut-off, etc. [1–4]. Eq. (1) corresponds to $\hat{\bar{\phi}}(\mathbf{k}_w, t) = \hat{G}(\mathbf{k}_w) \hat{\phi}(\mathbf{k}_w, t)$ in Fourier space, \mathbf{k}_w being the wavenumbers vector.

According to the Schumann's approach,⁵ filtering can be associated with a local average over an elementary box-volume [11,12,35] of linear homogeneous measure Δ . Thus, one can define the volume-averaged velocity in the continuous form

$$\bar{\mathbf{v}}(\mathbf{x}, t; \Delta) = \frac{1}{\Delta^3} \int_{z-\Delta/2}^{z+\Delta/2} dz' \int_{y-\Delta/2}^{y+\Delta/2} dy' \int_{x-\Delta/2}^{x+\Delta/2} dx' \mathbf{v}(\mathbf{x}', t) d\mathbf{x}'. \quad (2)$$

The filter parameter Δ is formally a degree of freedom in the filtering procedure. If the elementary volume is homogeneous, the (2) can be assimilated to the *top-hat* filtered velocity as it is possible to rewrite it in terms of the convolution product (1) with the filter kernel $1/|\Omega|$, $\forall \mathbf{x} \in \Omega$ and vanishing elsewhere. Note that the filtered velocity (2) still possesses an infinite number of Fourier components, its transfer function having an infinite number of zeros and vanishing asymptotically [1–4].

⁴ Stolz and co-authors [47] conclude that: “The minimum result to be expected from a LES is a good prediction of the mean flow. As can be seen from the strongly varying results obtained for different models this is in fact not easy to accomplish. In particular, many LES models fail to predict the near-wall behavior correctly”. For instance, solutions supplied with the standard Smagorinsky model overshoot the law of the wall significantly: the model is too dissipative near the wall and the predicted von Karman constant is too small. The shortcomings of the standard Smagorinsky model can be partially overcome by using the dynamic model, possibly in conjunction with an auxiliary equation for the SGS kinetic energy. However, in all cases, by using a finite-difference discretization the law of the wall is overshoot, the no-model LES surprisingly appearing as the best solution. As expected, all the results improve when the numerical resolution is increased. The mean velocity profiles obtained with the ADM procedure for coarsely and highly resolved LES with $Re_\tau = 180$ and 590 showed a very good agreement with the filtered DNS data. However, they claimed that: “the analytical form of the law of the wall is not necessarily invariant to a filter operation since the friction velocity of filtered data can be different from the unfiltered data”.

⁵ The Schumann's original paper describes the finite difference procedure and the SGS model with finite difference equations based on integral conservation equations for each grid volume. As a consequence, the SGS stresses are defined as surface mean rather than grid volume mean values of the fluctuating velocity products. There is no direct link to the Leonard's convolution filter paradigm.

In order to briefly clarify the matter, let us consider the simple one-dimensional counterpart of the exact transfer function of (2), that is $\hat{G}(k; \Delta) = \sin(k\Delta/2)/(k\Delta/2)$. This transfer function has infinite zeros, vanishing only for k going to infinity. On the other hand, when using a numerical method in practice, a computational grid of size h is introduced to discretize the domain. Consider the ideal case in which $\Delta = h$. Thus, considering only the action of the grid-filtering (that is a sharp cut-off), the transfer function would actually be truncated leading to $\hat{G}_g(k; h) \equiv [1 - H(k - k_c)]\hat{G}(k; h)$, H being the Heaviside function defined as $H(x) = \int_{-\infty}^x \delta(\xi) d\xi$ and $k_c = \pi/h$ the maximum resolvable wavenumber on the computational grid. However, the transfer function \hat{G}_g , would only represent an ideal case in which the continuous top-hat filtered velocity is sampled on the computational grid. In actual fact, a real numerical method implies using discrete grid-values. The effective shape of the transfer function is therefore induced by discretization.

The continuous governing equation for the large-scale velocity field $\bar{\mathbf{v}}$ is commonly obtained by applying the convolution (1) (or, equivalently, the averaging (2)) to each term of the Navier–Stokes (NS) equations, then commuting convolution and differential operators and supplying some SGS modeling for the unresolved terms arising from the non-linear flux. Then, for given boundary and initial conditions, a certain discretization in time and space allows us updating the LES solution. An explicit filtering operation is never actually performed in the solution algorithm but one lets the numerical discretization to induce implicitly the effective filter parameters. In fact, a real scale separation only appears after the discretization is introduced. This general philosophy appears straightforward but is the source of various interpretations in its practical application and analyses [1–10,16,18,24,25,51].

For the sake of simplicity, let us consider the Burgers multi-dimensional equation⁶ and apply the filtering to each term, which results in

$$\frac{\partial \bar{\mathbf{v}}}{\partial t} + \overline{\nabla \cdot \mathbf{F}(\mathbf{v})} = \mathbf{0}, \quad (3)$$

being $\mathbf{v}(\mathbf{x}, t)$ the point-wise velocity field, $\mathbf{F}(\mathbf{v}) = \mathbf{v}\mathbf{v} - 2\nu \nabla^s \mathbf{v}$ the total tensor flux, sum of the non-linear convective and the linear diffusive fluxes, respectively.

The key-point to highlight is that, in order to obtain the LES equation, commuting filtering and divergence operators in (3), that assumes $\overline{\nabla \cdot \mathbf{F}(\mathbf{v})} = \nabla \cdot \mathbf{F}(\bar{\mathbf{v}})$, is the common procedure in the LES community [1–4]. Moreover, when commutation property does not apply, one works using special commutative filters [1–4]. Thus, after introducing the decomposition in resolved $\mathbf{F}_R(\bar{\mathbf{v}}) = \bar{\mathbf{v}}\bar{\mathbf{v}} - 2\nu \nabla^s \bar{\mathbf{v}}$ and unresolved $\mathbf{F}_U(\bar{\mathbf{v}}, \mathbf{v}) = (\bar{\mathbf{v}}\mathbf{v} - \mathbf{v}\bar{\mathbf{v}})$ fluxes, the classical divergence form of the differential filtered equation is obtained,

$$\frac{\partial \bar{\mathbf{v}}}{\partial t} + \nabla \cdot \mathbf{F}_R(\bar{\mathbf{v}}) = \nabla \cdot \mathbf{F}_U(\bar{\mathbf{v}}, \mathbf{v}). \quad (4)$$

In order to close Eq. (4), the non-linear unresolved flux is modeled by introducing an approximation $\mathbf{F}_U(\bar{\mathbf{v}}, \mathbf{v}) \cong \mathbf{F}_{SGS}(\bar{\mathbf{v}})$.

On the other hand, numerical FV approximations which, according to the Reynolds Transport Theorem, start from the integral (weak) formulation of the conservation laws are analyzed in this study. We will never need to discretize the divergence operator but only the integral of the flux [11–15,17]. Thus, one writes the integral equation

$$\frac{\partial}{\partial t} \int_{\Omega(\mathbf{x})} \mathbf{v} d\mathbf{x}' + \int_{\partial\Omega(\mathbf{x})} \mathbf{n} \cdot \mathbf{F} dS(\mathbf{x}') = \mathbf{0}, \quad (5)$$

where Ω is an elementary volume, its frontier being denoted by $\partial\Omega$, \mathbf{n} being its unit vector, outward-oriented in normal direction. Owing to a proper decomposition of the flux \mathbf{F} in the resolved $\mathbf{F}_R(\bar{\mathbf{v}})$ and unresolved $\mathbf{T}(\bar{\mathbf{v}}, \mathbf{v}) = \mathbf{F}_R(\bar{\mathbf{v}}) - \mathbf{F}(\mathbf{v}) = (\bar{\mathbf{v}}\mathbf{v} - \mathbf{v}\bar{\mathbf{v}}) - (2\nu \nabla^s \bar{\mathbf{v}} - 2\nu \nabla^s \mathbf{v})$, a fundamental issue of the integral-based approach is that one does not demand commuting filtering and differentiation. The integral-based equation, governing the top-hat filtered velocity $\bar{\mathbf{v}}$, is written as

$$\frac{\partial \bar{\mathbf{v}}}{\partial t} + \overline{\nabla \cdot \mathbf{F}_R(\bar{\mathbf{v}})} = \overline{\nabla \cdot \mathbf{T}(\bar{\mathbf{v}}, \mathbf{v})}. \quad (6)$$

In order to close Eq. (6), the non-linear unresolved flux is modeled by introducing an approximation $\mathbf{T}(\bar{\mathbf{v}}, \mathbf{v}) \cong \mathbf{T}_{SGS}(\bar{\mathbf{v}})$. For the sake of clarity, the continuous equation (6) is rewritten in its actual integral-based counterpart form that will be used for analyzing the FV discretizations

$$\frac{\partial \bar{\mathbf{v}}}{\partial t} + \frac{1}{|\Omega|} \int_{\partial\Omega} \mathbf{n} \cdot \mathbf{F}_R(\bar{\mathbf{v}}) dS = \frac{1}{|\Omega|} \int_{\partial\Omega} \mathbf{n} \cdot \mathbf{T}(\bar{\mathbf{v}}, \mathbf{v}) dS \cong \frac{1}{|\Omega|} \int_{\partial\Omega} \mathbf{n} \cdot \mathbf{T}_{SGS}(\bar{\mathbf{v}}) dS. \quad (7)$$

Bearing in mind such equivalence, using integral (7) or over-bar symbolism (6) will depend on the necessity of exposition.

To conclude this section, from a comparison of Eqs. (4) and (6), one can see that, even if the resolved flux \mathbf{F}_R is the same, the unresolved flux \mathbf{T} is very different from \mathbf{F}_U both in the non-linear part and in the presence of the residual diffusive flux. Furthermore, only if the same top-hat one filter function G is prescribed would Eqs. (4) and (6) then be formally equivalents, both governing the same filtered velocity. Perhaps, defining a filter type for Eq. (4) is only a formalism. In fact, the filtering operation is never explicitly introduced (unless using an explicit filtering formulation). Thus if one specified some other filter

⁶ Contrary to the definition used by other authors, e.g. see Ref. [11], as “multidimensional” Burgers equation is here denoted nothing else than the momentum equation for homogeneous density while disregarding the pressure term.

function, such as the Gaussian or the spectral cut-off filter, it would leave (4) unchanged. In practice, Eq. (4) does not allow us to univocally identify the type of induced filter being it driven only by the used expression of the SGS model. Conversely, Eq. (6) univocally implies only the application of the volume average-based filtering since it is characterized by the presence of resolved and unresolved fluxes under explicit surface integrals.

3. Integral versus differential-based filtered formulations in discrete form: an analysis of implicit filtering in FV and FD methods

The introduction of numerical discretizations highlights the difference between FV and FD approaches. While using implicit filtering-based approaches, both the computational grid and the discretization of the operators implicitly act as filtering to the equations [1–6,8,18,24]. Hence, let us assume a computational grid of homogeneous size h and denote with $\overline{\nabla \cdot (*)}^d$ a certain type of FV-based spatial discretization (from now on, superscript d will denote only spatial discretization). According to the genuine FV approach [11,12,40], the above discrete operator consists of the numerical approximation to the integral of the fluxes over the surfaces of the FV. The discretization of Eq. (6) defines the evolution of the discrete filtered velocity, say $\tilde{\mathbf{v}}^d$, that is

$$\frac{\partial \tilde{\mathbf{v}}^d}{\partial t} + \overline{\nabla \cdot \mathbf{F}_R^d(\tilde{\mathbf{v}}^d)}^d = \overline{\nabla \cdot \mathbf{T}_{SGS}^d(\tilde{\mathbf{v}}^d)}^d, \quad (8)$$

having defined the discrete resolved total flux $\mathbf{F}_R^d = \tilde{\mathbf{v}}^d \tilde{\mathbf{v}}^d - 2\nu \nabla^d \tilde{\mathbf{v}}^d$. Owing both to the specific flux decomposition [15,17,42] and to the numerical character of the unresolved tensor stress [8,16,18,21,24,25], the use of the integral-based LES equation (8) affects also the choice of the SGS modeling.

The velocity $\tilde{\mathbf{v}}^d$ is now representative of a finite-dimensional state-vector, possessing only a finite numbers of resolved length scales, bounded by the smallest computational size associated with the Nyquist frequency h/π .⁷ In actual fact, the resolved Fourier components of $\tilde{\mathbf{v}}^d$ also contain the smoothing induced by the shape of the implicit filtering that depends on the type of discretization of $\overline{\nabla \cdot (*)}^d$. Note that in this study we did not use deconvolution procedures to improve the spectral resolution of the filtered velocity, see Refs. [13,14,30,34,35]. Thus, in order to understand the real resolution of the velocity $\tilde{\mathbf{v}}^d$, recognizing the effective implicit filtering underlying the entire FV discretization is a fundamental task. For example, it is well known that a linear flux reconstruction leads to a central second order derivative-like [1,6]. In the Fourier space one deduces that the numerical transfer function $\hat{G}_d(k; h) \equiv [1 - H(k - k_c)] \sin(kh)/(kh)$ is induced. Thus, \hat{G}_d turns to be the resulting numerical approximation to \hat{G}_g , which is induced by both the domain and operators discretization. Consequently, the ideal filter length $\Delta = h$ is not achieved, the induced numerical transfer function \hat{G}_d being equal to \hat{G}_g for $\Delta = 2h$. This example justifies the introduction of the *sub-filter resolution parameter* $Q = \Delta/h$.

On the other hand, classic LES solutions are based on the common discretization of (4) (the divergence form is sometimes substituted by the skew-symmetric or rotational counterpart), that is

$$\frac{\partial \tilde{\mathbf{v}}^d}{\partial t} + \overline{\nabla^d \cdot \mathbf{F}_R^d(\tilde{\mathbf{v}}^d)}^d = \overline{\nabla^d \cdot \mathbf{T}_{SGS}^d(\tilde{\mathbf{v}}^d)}^d. \quad (9)$$

It is worthwhile noticing that, although clearly distinct from (8), the above FD-based discretization is often also denoted in literature as FV discretization (see Refs. [16,24]). The discrete equations (8) and (9) actually differ greatly since, for the latter, a discretization formula $\overline{\nabla^d \cdot (*)}^d$ does not necessarily induce an approximation to the exact top-hat transfer function, as reviewed in Refs. [1,6,13,14,24] and will be further detailed in Section 3.4. Unlike Eqs. (8) and (9) does not univocally define a⁸ type of numerically induced filter function (for example, (9) can be used assuming the spectral cut-off filter). Generally, this ambiguity concerning the type of filtering is reflected in the sub-filter stress that contains the full information on the filter. In other words, defining an SGS model for the unresolved tensor is equivalent to defining a filter function [16,18,22,24,25].

The ambiguity in discerning the shape of the implicit filtering as well as the goal of more effectively controlling the numerical errors suggest using the so-called *explicit filtering technique* (see Refs. [5–9,51]). This technique is implemented either by explicitly applying some supplementary filter on the non-linear resolved flux, that is by computing $\overline{\nabla^d \cdot (\tilde{\mathbf{v}}^d \tilde{\mathbf{v}}^d)}$, or explicitly filtering the resolved velocity field at each (or some multiple) time step, i.e. by computing $\tilde{\mathbf{v}}^d$. However, even if one used a volume average-based filtering, filtering in such a way would not be linked with the use of the integral conservation law.

3.1. Integral-based discretization and the filtering error in physical space

In this sub-section, the FV-based approximation is introduced. The key-point is that using the integral-based discretization, filtering (i.e. the integral of the fluxes) is applied outside the divergence operator, in a sort of explicit filter arrangement.

⁷ The resolved discrete convective flux is formed by the product of the finite-dimensional vectors $\tilde{\mathbf{v}}^d$, and “aliased” frequencies could therefore appear. However, like the sampling of the velocity, the non-linear flux is itself sampled on the computational grid. It possesses a finite numbers of length scales, bounded by the Nyquist frequency, and affected by the shape of the implicit filtering.

⁸ Strictly speaking, one should distinguish between the class of discrete filtered velocity $\tilde{\mathbf{v}}^d$ for either FD or FV discretizations. However, in order not to complicate the notation, no other symbols will be used.

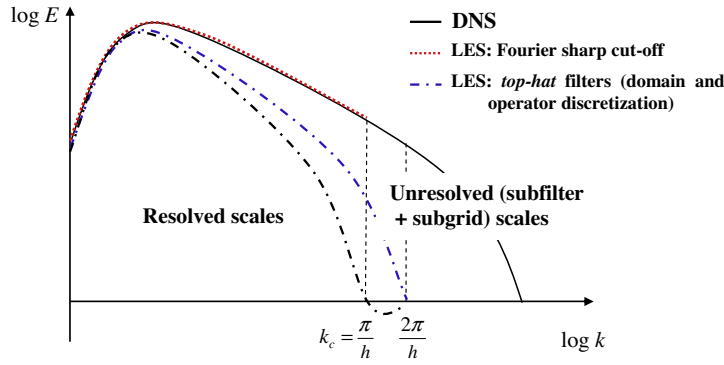


Fig. 1b. This graphical sketch depicts the scales separation that is induced by an implicit FV-based filtering. Here k_c represents the grid cut-off wavenumber, implicitly associated to a domain discretization, that lets unaffected the energy content up to k_c . For a given computational grid size h , the transfer function induced by a FV discretization is supposed in the form $[1 - H(k - k_c)]\sin(kQh/2)/(kQh/2)$. As addressed in the text, the case $Q = 1$ (blue line) corresponds to the ideal FV transfer function for which the first zero lies over the Nyquist frequency. For $Q = 2$ (black line), the first zero coincides with the Nyquist frequency and the figure well represents the case of the 1D central second order flux reconstruction. (For interpretation of the references in colour in this figure legend, the reader is referred to the web version of this article.)

The consequence is that a numerical transfer function approximating uniquely the top-hat filter is expected. For the sake of simplicity, one disregards in the following equation the contribution of the SGS terms.

According to a typical FV-based flux reconstruction [11,12] on a Cartesian computational grid of homogeneous step size h , the discrete equations (8) is rewritten as

$$\frac{\partial \bar{\mathbf{v}}^d}{\partial t} = -\bar{\nabla} \cdot \bar{\mathbf{F}}_R^d = -\frac{1}{h^3} \sum_{i=1}^3 I_{|x_j-h/2}^{x_j+h/2} I_{|x_k-h/2}^{x_k+h/2} \left(\bar{\mathbf{f}}_{R,x_i}^d \Big|_{x_i+h/2} - \bar{\mathbf{f}}_{R,x_i}^d \Big|_{x_i-h/2} \right) \equiv -\sum_{i=1}^3 \frac{\delta \bar{\mathbf{f}}_{R,x_i}^d}{\delta x_i}, \quad (j, k = 1, 2, 3; i \neq j \neq k), \quad (10)$$

having defined with $I_{|x_j-h/2}^{x_j+h/2}$ a discrete surface integrals operator acting on the discrete flux $\bar{\mathbf{f}}_{R,x_i}^d = \bar{u}_i \bar{\mathbf{v}} - \nu \frac{\partial \bar{\mathbf{v}}}{\partial x_i}$, u_i being the Cartesian velocity components and denoting δ_{x_i} a discrete derivative operator along the i th direction.

Two factors which both determine the length and shape of the filter induced by the discretization can be addressed: the order of accuracy of the discrete flux reconstruction and the type of collocation (staggered or not) of the velocity components on the computational grid. Note that the continuous integral conservation law was written over a volume of characteristic linear width Δ . Hence, one can quite reasonably suppose that Eq. (10) produces a numerical transfer function approximating the top-hat filter over an effective filter length which is some multiplier Q of the mesh size h . This length will be denoted as $\Delta_{eff} = Qh$, the “effective” filter width. Introducing a unique scalar parameter Q is fully justified only if a unique computational length h and homogenous discretization is used (as happens in the case of homogeneous turbulence simulations). Alternatively, it would be more suitable to assume a vector of scalars Q_i . The *sub-filter resolution* parameter Q has a value of ≥ 1 and it is known to strongly affect the computed statistics (see Refs. [24,45]). Fig. 1b provides a graph showing the action of the implicit filtering on a typical turbulence spectrum. Only scales below h are effectively removed by the effect of the Nyquist cut-off associated with the grid-filter. Marginal resolution of the numerical method produces scales lying between Δ_{eff} and h that, which are differently resolved depending on value of Q . The coarseness of the discretization produces a dynamic contribution, i.e. additional small-scale effects in (12) arising from the built-in filtering. Consequently, any SGS closure modeling should take into account the level of the real filter, as well as the difference between the “ideal” unresolved turbulent stress and the “computational” turbulent stress tensor [5,8,9,13,16,24,45].

In order to analyze (12), the continuous integral conservation law is firstly rewritten (while disregarding the SGS term) over a Cartesian box of homogeneous linear length Δ_{eff} , which is explicitly linked to the parameter Q and grid size h

$$\frac{\partial \bar{\mathbf{v}}^{\Delta_{eff}}}{\partial t} = -\frac{1}{(Qh)^3} \sum_{i=1}^3 \int_{x_k-Qh/2}^{x_k+Qh/2} dx'_k \int_{x_j-Qh/2}^{x_j+Qh/2} \mathbf{n}_i \cdot (\bar{\mathbf{F}}_R|_{x_i+Qh/2} - \bar{\mathbf{F}}_R|_{x_i-Qh/2}) dx'_j \equiv -\sum_{i=1}^3 \frac{\partial \bar{\mathbf{f}}_{R,x_i}^{\Delta_{eff}}}{\partial x_i}, \quad (j, k = 1, 2, 3; i \neq j \neq k), \quad (11)$$

where $\bar{\mathbf{v}}^{\Delta_{eff}}(\mathbf{x}, t) = \bar{\mathbf{v}}(\mathbf{x}, t; \Delta = Qh)$, having denoted with \mathbf{n}_i , the unit vectors along the x , y and z -axes, respectively. The continuous resolved flux is $\bar{\mathbf{F}}_R(\bar{\mathbf{v}}^{\Delta_{eff}}) = \bar{\mathbf{v}}^{\Delta_{eff}} \bar{\mathbf{v}}^{\Delta_{eff}} - 2\nu \bar{\nabla}^S \bar{\mathbf{v}}^{\Delta_{eff}}$, its resolved vector component being $\bar{f}_{R,x_i}^{\Delta_{eff}} = \bar{u}_i^{\Delta_{eff}} \bar{\mathbf{v}}^{\Delta_{eff}} - \nu \frac{\partial \bar{\mathbf{v}}^{\Delta_{eff}}}{\partial x_i}$. The notation introduced above may appear redundant; but it is adopted in order to highlight the fact that, since the only input length in LES is the mesh size h , the integration method solves for a finite-dimensional vector $\bar{\mathbf{v}}^d$ which can be seen as an approximation of the continuous filtered velocity⁹ $\bar{\mathbf{v}}^{\Delta_{eff}}$.

An analysis of Eqs. (8) and (6) provides us with a way to estimate the differences between the exact and (spatially) discrete filtered acceleration fields, that is $\frac{\partial \bar{\mathbf{v}}^{\Delta_{eff}}}{\partial t} - \frac{\partial \bar{\mathbf{v}}^d}{\partial t}$. However, this difference makes sense only at a fixed time and in a discrete

⁹ The filtered velocity $\bar{\mathbf{v}}^{\Delta_{eff}}(\mathbf{x}, t)$ would, in actual fact, be an exact solution of (11) only by adding the unresolved terms.

sense, as it is necessary to sample the exact derivative $\partial_t \bar{\mathbf{v}}^{\Delta_{\text{eff}}}(\mathbf{x}, t)$ over the computational nodes. The difference of the discrete vectors (which can be considered as a sort of discretization error [11,12]) can be written according to

$$\frac{\partial \bar{\mathbf{v}}^{\Delta_{\text{eff}}}}{\partial t} - \frac{\partial \bar{\mathbf{v}}^d}{\partial t} = - \left[\left(\overline{\nabla \cdot (*)^{\Delta_{\text{eff}}}} - \overline{\nabla \cdot (*)^d} \right) \mathbf{F}_R + \overline{\nabla \cdot (\mathbf{F}_R - \mathbf{F}_R^d)^d} \right] + \left[\overline{\nabla \cdot \mathbf{T}(\bar{\mathbf{v}}^{\Delta_{\text{eff}}}, \mathbf{v})^{\Delta_{\text{eff}}}} - \overline{\nabla \cdot \mathbf{T}_{\text{SGS}}^d} \right]. \quad (12)$$

The RHS of (12) highlights some specific contributions in square brackets. Two terms in the first brackets are respectively:

- the difference between the continuous and the discrete filtered divergence operators applied on the resolved continuous flux F_R ,¹⁰ i.e. the classic local truncation error [11,12] (LTE) due to the FV discretization;
- the discrete integral applied to the difference between the continuous \mathbf{F}_R and the discrete \mathbf{F}_R^d resolved total fluxes (this term can be seen as due to a “sampling filtering” effect; the \mathbf{F}_R flux is sampled on the computational grid, and therefore possesses a finite number of length scales).

The second square brackets contain the difference between modeling and discretization of the SGS term. It could be further expressed by means of two concurrent contributions, highlighting the so-called *computational turbulent stress tensor*, which is the full closure problem at the level of the effective spatial discretization [15,17]. Thus, disregarding the SGS contribution, the error expression (12) is written in a compact index notation (no summation implied)

$$\begin{aligned} e_{ij}^{\Delta_{\text{eff}}} &= \frac{\overline{\partial \left(\bar{u}_i^{\Delta_{\text{eff}}} \bar{u}_j^{\Delta_{\text{eff}}} - v \partial \bar{u}_i^{\Delta_{\text{eff}}} / \partial x_j \right)^{\Delta_{\text{eff}}}}}{\partial x_j} - \frac{\overline{\partial \left(\bar{u}_i^d \bar{u}_j^d - v \partial \bar{u}_i^d / \partial x_j \right)^d}}{\partial x_j} \\ &= \left(\frac{\partial}{\partial x_j} - \frac{\partial^d}{\partial x_j} \right) \left(\bar{u}_i^{\Delta_{\text{eff}}} \bar{u}_j^{\Delta_{\text{eff}}} - v \partial \bar{u}_i^{\Delta_{\text{eff}}} / \partial x_j \right) + \frac{\partial^d}{\partial x_j} \left[\left(\bar{u}_i^{\Delta_{\text{eff}}} \bar{u}_j^{\Delta_{\text{eff}}} - v \partial \bar{u}_i^{\Delta_{\text{eff}}} / \partial x_j \right) - \left(\bar{u}_i^d \bar{u}_j^d - v \partial \bar{u}_i^d / \partial x_j \right) \right]. \end{aligned} \quad (13)$$

The analysis of (13) is illustrated in the following subsections.

3.2. Continuous and discrete filtered velocity and the resolved fluxes in wavenumber space

According to other studies [20–24], the analysis of (13) in terms of the sub-filter parameter Q is better suited to Fourier space. First, the ideal continuous point-wise velocity is introduced in terms of the Fourier series as $\mathbf{v}(\mathbf{x}) = \sum_{k_x=-\infty}^{+\infty} \sum_{k_y=-\infty}^{+\infty} \sum_{k_z=-\infty}^{+\infty} \hat{\mathbf{v}}(\mathbf{k}_w) e^{i\mathbf{k}_w \cdot \mathbf{x}} \equiv \sum_{k_x, k_y, k_z}^{\pm\infty} \hat{\mathbf{v}}(\mathbf{k}_w) e^{i\mathbf{k}_w \cdot \mathbf{x}}$, the wavenumber vector being $\mathbf{k}_w = i\mathbf{k}_x + j\mathbf{k}_y + k\mathbf{k}_z$. Here, the capital letter I is used to denote the imaginary unit. Fourier coefficients in the series are absolutely integrable functions of \mathbf{v} .

A hierarchical sequence of filtered velocity fields [36] is then introduced in terms of the above Fourier series. According to the convolution product (2), the continuous top-hat filtered velocity field $\bar{\mathbf{v}}^{\Delta_{\text{eff}}}$ is written as

$$\begin{aligned} \bar{\mathbf{v}}^{\Delta_{\text{eff}}}(\mathbf{x}) &= \frac{1}{(Qh)^3} \int_{x-Qh/2}^{x+Qh/2} dx' \int_{y-Qh/2}^{y+Qh/2} dy' \int_{z-Qh/2}^{z+Qh/2} dz' \sum_{k_x, k_y, k_z}^{\pm\infty} \hat{\mathbf{v}}(\mathbf{k}_w) e^{i\mathbf{k}_w \cdot \mathbf{x}'} \\ &= \sum_{k_z=-\infty}^{+\infty} \sum_{k_y=-\infty}^{+\infty} \sum_{k_x=-\infty}^{+\infty} \hat{G}(k_x; \Delta_{\text{eff}}) \hat{G}(k_y; \Delta_{\text{eff}}) \hat{G}(k_z; \Delta_{\text{eff}}) \hat{\mathbf{v}}(\mathbf{k}_w) e^{i\mathbf{k}_w \cdot \mathbf{x}} \\ &= \left[\sum_{k_z=-k_{z,\text{max}}}^{k_{z,\text{max}}} \sum_{k_y=-k_{y,\text{max}}}^{k_{y,\text{max}}} \sum_{k_x=-k_{x,\text{max}}}^{k_{x,\text{max}}} \hat{G}_{\mathbf{x}}(k_x, k_y, k_z; \Delta_{\text{eff}}) + \sum_{k_z}^{\text{other}} \sum_{k_y}^{\text{other}} \sum_{k_x}^{\text{other}} \hat{G}_{\mathbf{x}}(k_x, k_y, k_z; \Delta_{\text{eff}}) \right] \hat{\mathbf{v}}(\mathbf{k}_w) e^{i\mathbf{k}_w \cdot \mathbf{x}} \\ &= \sum_{k_x, k_y, k_z} \widehat{\bar{\mathbf{v}}^{\Delta_{\text{eff}}}}(\mathbf{k}_w) e^{i\mathbf{k}_w \cdot \mathbf{x}} + \sum_{k_x, k_y, k_z}^{\text{other}} \widehat{\bar{\mathbf{v}}^{\Delta_{\text{eff}}}}(\mathbf{k}_w) e^{i\mathbf{k}_w \cdot \mathbf{x}} \equiv \bar{\mathbf{v}}_R^{\Delta_{\text{eff}}}(\mathbf{x}) + \bar{\mathbf{v}}_U^{\Delta_{\text{eff}}}(\mathbf{x}), \end{aligned} \quad (14)$$

having defined the 1D transfer function $\hat{G}(\chi; \Delta_{\text{eff}}) \equiv \sin(\chi \Delta_{\text{eff}}/2)/(\chi \Delta_{\text{eff}}/2) = \sin(\chi Qh/2)/(\chi Qh/2)$ and the factorized multi-dimensional transfer function $\hat{G}_{\mathbf{x}}(k_x, k_y, k_z; \Delta_{\text{eff}}) \equiv \hat{G}(k_x; \Delta_{\text{eff}}) \hat{G}(k_y; \Delta_{\text{eff}}) \hat{G}(k_z; \Delta_{\text{eff}})$ (which is depicted in Fig. 2). Consequently, the filtered Fourier coefficients are $\bar{\mathbf{v}}^{\Delta_{\text{eff}}}(\mathbf{k}_w) \equiv \hat{G}_{\mathbf{x}}(k_x, k_y, k_z; \Delta_{\text{eff}}) \hat{\mathbf{v}}(\mathbf{k}_w)$.

An infinite number of Fourier coefficients has been considered for the filtered velocity (14) since it is assumed to satisfy exactly the continuous integral conservation law (3). Hence, Eq. (14) should only be considered only as the “ideal” top-hat filtered velocity. In fact, in a practical LES, the computed discrete filtered velocity vector $\bar{\mathbf{v}}^d$ has a finite number of resolved components. The resolvable and irresolvable parts of (14) were therefore introduced, denoted as $\bar{\mathbf{v}}_R^{\Delta_{\text{eff}}}(\mathbf{x})$ and $\bar{\mathbf{v}}_U^{\Delta_{\text{eff}}}(\mathbf{x})$, respectively. The velocity field $\bar{\mathbf{v}}_R^{\Delta_{\text{eff}}}(\mathbf{x})$ is substantially the truncated Fourier series that can be substituted by its integral representation as a convolution of the function $\bar{\mathbf{v}}^{\Delta_{\text{eff}}}$ with the *Dirichlet kernel* [36,37]. Indeed, by performing the inverse Fourier transforms of $\hat{G}_{\mathbf{x}}(p, q, r; \Delta_{\text{eff}})$ along each x_k direction, it is a simple task to deduce the filter kernels $G_{\mathbf{x}}$ corresponding to the exact top-hat filtered velocity (14)

¹⁰ A discrete operator applied to a continuous function is, of course, considered as being applied to the discrete values that the function assumed on the same computational nodes where the numerical solution is computed.

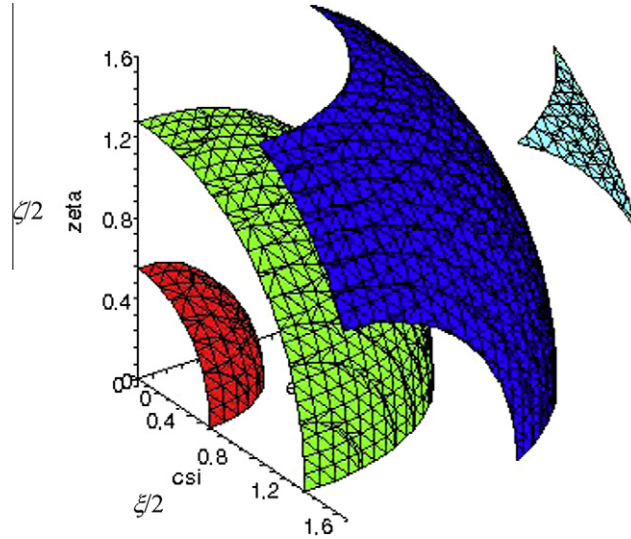


Fig. 2. Sampling of four iso-value surfaces at 0.35, 0.55, 0.75, 0.95 in cyan, blue, green and red colors, respectively, representing the exact FV-based transfer function \hat{G}_x . (For interpretation of the references in colour in this figure legend, the reader is referred to the web version of this article.)

$$\hat{G}_x(\mathbf{x} - \mathbf{x}'; \Delta_{\text{eff}}) = \frac{1}{(Qh)^3} \prod_{k=1}^3 \left[H\left(x_k - x'_k - \frac{Qh}{2}\right) - H\left(x_k - x'_k + \frac{Qh}{2}\right) \right], \quad (15)$$

the Heaviside function being $H(x_k - x'_k \pm \frac{Qh}{2})$. In actual fact, the Fourier inverse transform of the truncated transfer function $\hat{G}_x(p, q, r; \Delta_{\text{eff}}) \prod_{k=1}^3 [H(p_k - p_{k,\text{max}})H(-p_k - p_{k,\text{max}})]$ should be made. As a result, (15) does not exactly define the filter kernel of the velocity field $\hat{\mathbf{v}}_R^{\Delta_{\text{eff}}}(\mathbf{x})$. Of course, $\hat{\mathbf{v}}_R^{\Delta_{\text{eff}}}(\mathbf{x})$ does not exactly obey the integral form of the conservation law (3) but it can still be seen as a solution for a “weak form” obtained by means of a projection along suitable test-functions (see Refs. [2,11,37]). On the other hand, the field $\hat{\mathbf{v}}_U^{\Delta_{\text{eff}}}(\mathbf{x})$, composed of an infinite number of irresolvable Fourier components, is the part responsible for the SGS terms.

Therefore, by assuming that the discrete velocity components are prescribed on the computational grid, the velocity $\hat{\mathbf{v}}^d$ is reconstructed in a continuous form according to the three-dimensional Fourier polynomial $P_F^3 \hat{\mathbf{v}}^d(\mathbf{x})$

$$\begin{aligned} P_F^3 \hat{\mathbf{v}}^d(\mathbf{x}) &\equiv \sum_{r=-N_z/2}^{N_z/2-1} \sum_{q=-N_y/2}^{N_y/2-1} \sum_{p=-N_x/2}^{N_x/2-1} \hat{\mathbf{v}}^d(\mathbf{k}_w) e^{i\mathbf{k}_w \cdot \mathbf{x}} = \sum_{r=-r_{\text{max}}}^{r_{\text{max}}-1} \sum_{q=-q_{\text{max}}}^{q_{\text{max}}-1} \sum_{p=-p_{\text{max}}}^{p_{\text{max}}-1} \hat{\mathbf{v}}^d(p, q, r) e^{i(px+qy+rz)} \\ &\equiv \sum_{p,q,r} \hat{\mathbf{v}}^d(p, q, r) e^{i(px+qy+rz)}, \end{aligned} \quad (16)$$

having defined N_x, N_y, N_z as even positive integers and $k_x = 2\pi p/L_x, k_y = 2\pi q/L_y, k_z = 2\pi r/L_z$. The function is assumed periodic over a box of length $L_x = L_y = L_z = 2\pi \equiv L$, which is discretized by a uniform grid of $N_x = N_y = N_z = N$ points, $h = L/N$ being the step-size. Hence, one has $k_x = p, k_y = q, k_z = r$ and the summations in (16) extend until the values $p_{\text{max}} = q_{\text{max}} = r_{\text{max}} = \pi/h = N/2$, corresponding to the Nyquist frequencies along x, y and z directions, respectively. The use of polynomial (16) allows us to highlight the following issues:

- (1) The resolvable part of the filtered velocity $\hat{\mathbf{v}}_R^{\Delta_{\text{eff}}}(\mathbf{x})$ has the same number of Fourier components as $P_F^3 \hat{\mathbf{v}}^d(\mathbf{x})$, allowing a congruent comparison to be made.
- (2) The Fourier coefficients $\hat{\mathbf{v}}^d(p, q, r)$ (these can be computed solving a classical algebraic system) implicitly contain the shape of the numerical transfer function induced by the FV method adopted. The induced smoothing can be different from that in (14).

According to previous definitions, the “ideal” filtered fluxes, which will be used as exact comparison terms in the error expression (13), can be written in the Fourier space. For example, while fixing $j = 1$ and using (14), the x -direction convective flux component is

$$\begin{aligned} \frac{\partial (\bar{u}^{\Delta_{\text{eff}}} \bar{u}_i^{\Delta_{\text{eff}}})}{\partial x} &= \frac{1}{(Qh)^3} \int_{z-Qh/2}^{z+Qh/2} d\zeta \int_{y-Qh/2}^{y+Qh/2} \left(\bar{u}^{\Delta_{\text{eff}}} \bar{u}_i^{\Delta_{\text{eff}}} \Big|_{x+Qh/2} - \bar{u}^{\Delta_{\text{eff}}} \bar{u}_i^{\Delta_{\text{eff}}} \Big|_{x-Qh/2} \right) d\eta \\ &= I \sum_{l,m,n}^{\pm\infty} \sum_{p,q,r}^{\pm\infty} p' \hat{G}_x(p', q', r'; \Delta_{\text{eff}}) \hat{u}^{\Delta_{\text{eff}}}(p, q, r) \hat{u}_i^{\Delta_{\text{eff}}}(l, m, n) e^{i(p'x+q'y+r'z)}, \end{aligned} \quad (17)$$

having defined $p' \equiv (p + l)$, $q' \equiv (q + m)$, $r' \equiv (r + n)$. It is straightforward to extend (17) to the other filtered convective fluxes along y - and z -directions, writing them in a compact index notation (no summation is implied) according to

$$\frac{\partial(\bar{u}_j^{\Delta_{eff}} \bar{u}_i^{\Delta_{eff}})}{\partial x_j} = I \sum_{l,m,n}^{\pm\infty} \sum_{p,q,r}^{\pm\infty} p'_j \widehat{G}_x(p', q', r'; \Delta_{eff}) \widehat{\bar{u}_j^{\Delta_{eff}}}(p, q, r) \widehat{\bar{u}_i^{\Delta_{eff}}}(l, m, n) e^{I \sum_{k=1}^3 p'_k x_k}, \quad (18)$$

having denoted the wavenumbers $p' \equiv p'_1$, $q' \equiv p'_2$, $r' \equiv p'_3$.

Similarly, one works for the x -direction diffusive flux component, which results in

$$\begin{aligned} \frac{\partial}{\partial x} \left(v \frac{\partial \bar{u}_i^{\Delta_{eff}}}{\partial x} \right) &= \frac{v}{(Qh)^3} \int_{z-Qh/2}^{z+Qh/2} d\zeta \int_{y-Qh/2}^{y+Qh/2} \left(\frac{\partial \bar{u}_i^{\Delta_{eff}}}{\partial \zeta} \bigg|_{x+Qh/2} - \frac{\partial \bar{u}_i^{\Delta_{eff}}}{\partial \zeta} \bigg|_{x-Qh/2} \right) d\eta \\ &= -v \sum_{l,m,n}^{\pm\infty} l^2 \widehat{G}_x(l, m, n; \Delta_{eff}) \widehat{\bar{u}_i^{\Delta_{eff}}}(l, m, n) e^{I(lx+my+nz)}. \end{aligned} \quad (19)$$

A generic component of the diffusive flux is written as

$$\frac{\partial}{\partial x_j} \left(v \frac{\partial \bar{u}_i^{\Delta_{eff}}}{\partial x_j} \right) = -v \sum_{l,m,n}^{\pm\infty} l_j^2 \widehat{G}_x(l, m, n; \Delta_{eff}) \widehat{\bar{u}_i^{\Delta_{eff}}}(l, m, n) e^{I \sum_{k=1}^3 l_k x_k}, \quad (20)$$

having denoted the wavenumbers $l \equiv l_1$, $m \equiv l_2$, $n \equiv l_3$.

Finally, one can rewrite the i th component of Eq. (11) according to

$$\begin{aligned} \frac{\partial \bar{u}_i^{\Delta_{eff}}}{\partial t} &= - \sum_{j=1}^3 \frac{\partial(\bar{u}_j^{\Delta_{eff}} \bar{u}_i^{\Delta_{eff}} - v \partial \bar{u}_i^{\Delta_{eff}} / \partial x_j)}{\partial x_j} \\ &= -I \sum_{l,m,n}^{\pm\infty} \sum_{p,q,r}^{\pm\infty} \left[\sum_{j=1}^3 p'_j \widehat{G}_x(p', q', r'; \Delta_{eff}) \widehat{\bar{u}_j^{\Delta_{eff}}}(p, q, r) \right] \widehat{\bar{u}_i^{\Delta_{eff}}}(l, m, n) e^{I \sum_{k=1}^3 p'_k x_k} \\ &\quad - v \sum_{l,m,n}^{\pm\infty} \sum_{j=1}^3 l_j^2 \widehat{G}_x(l, m, n; \Delta_{eff}) \widehat{\bar{u}_i^{\Delta_{eff}}}(l, m, n) e^{I \sum_{k=1}^3 l_k x_k}. \end{aligned} \quad (21)$$

Therefore, Eqs. (18), (19) and (21) are the elements allowing us to perform the comparison between the FV-based and the exact integral-based top-hat filtered equations.

For the sake of completeness, the differential divergence form of the filtered equation is also considered, i.e. Eq. (4), disregarding the SGS terms. Specifically, the divergence of the resolved convective flux is

$$\frac{\partial(\bar{u}_j^{\Delta_{eff}} \bar{u}_i^{\Delta_{eff}})}{\partial x_j} = I \sum_{l,m,n}^{\pm\infty} \sum_{p,q,r}^{\pm\infty} p'_j \widehat{u}_j^{\Delta_{eff}}(p, q, r) \widehat{\bar{u}_i^{\Delta_{eff}}}(l, m, n) e^{I \sum_{k=1}^3 p'_k x_k} \quad (22)$$

and the divergence of the diffusive flux is

$$\frac{\partial}{\partial x_j} \left(v \frac{\partial \bar{u}_i^{\Delta_{eff}}}{\partial x_j} \right) = -v \sum_{l,m,n}^{\pm\infty} l_j^2 \widehat{\bar{u}_i^{\Delta_{eff}}}(l, m, n) e^{I \sum_{k=1}^3 l_k x_k}. \quad (23)$$

Hence, one writes the i th scalar component of the differential equation (4)

$$\begin{aligned} \frac{\partial \bar{u}_i^{\Delta_{eff}}}{\partial t} &= - \sum_{j=1}^3 \frac{\partial(\bar{u}_j^{\Delta_{eff}} \bar{u}_i^{\Delta_{eff}} - v \partial \bar{u}_i^{\Delta_{eff}} / \partial x_j)}{\partial x_j} \\ &= -I \sum_{l,m,n}^{\pm\infty} \sum_{p,q,r}^{\pm\infty} \left[\sum_{j=1}^3 p'_j \widehat{u}_j^{\Delta_{eff}}(p, q, r) \right] \widehat{\bar{u}_i^{\Delta_{eff}}}(l, m, n) e^{I \sum_{k=1}^3 p'_k x_k} - v \sum_{l,m,n}^{\pm\infty} \sum_{j=1}^3 l_j^2 \widehat{\bar{u}_i^{\Delta_{eff}}}(l, m, n) e^{I \sum_{k=1}^3 l_k x_k}. \end{aligned} \quad (24)$$

3.3. An analysis of the transfer functions induced by some FV schemes

Some common FV-based discretizations of different accuracy order, with staggered and non-staggered collocation of the velocity components, are addressed in this section. Hence, the three-dimensional transfer functions, induced by each spatial discretization, are deduced. Then, the approximation in terms of the sub-filter parameter Q is analyzed.

3.3.1. Two classical second order accurate central reconstructions on non-staggered grid: flux and velocity reconstruction

The simplest way to get a second order accurate flux reconstruction is obtained by *mean value formula* for the discrete integral operators, that is $I_{x_i-h/2}^{x_i+h/2} f = f(x_i)h$, and the *linear interpolation* for evaluating the flux on the mid-point [11,12]. Such an approach is perhaps the source of some misunderstanding since, for linear equations, this FV method results in the same algebraic coefficients of the second order centered FD-based discretization [12]. Traditionally, this kind of discretization is often used in the LES community to justify implicit top-hat filtering.

When a non-staggered collocation is chosen, solving the Navier–Stokes equations for incompressible flows at second order of accuracy in space requires some care in order to produce both divergence-free and oscillation-free solutions [12,15,17,26]. Moreover, setting the central reconstruction compels us to choose between two possible methods to evaluate the mean value of the convective flux. The first option is to simply perform the linear interpolation of the velocity product by exploiting two adjacent nodes across the direction normal to the integration surface. This scheme will be denoted as *NSF* (Non-Staggered Flux) reconstruction, adding the subscript *c* or *d* to denote the convective and the diffusive terms respectively. For example, while fixing $j = 1$, by using the Fourier polynomial (16), one can write the numerically filtered convective flux $\bar{u}^d \bar{u}_i^d$ according to

$$\begin{aligned} \left(\frac{\delta(\bar{u}^d \bar{u}_i^d)}{\delta x} \right)_{NSF} &\triangleq NSF_{c,i1}^d = \frac{1}{h^3} \left[(\bar{u}^d \bar{u}_i^d)|_{x+h/2,y,z} h^2 - (\bar{u}^d \bar{u}_i^d)|_{x-h/2,y,z} h^2 \right] \\ &= \frac{1}{h} \left\{ \frac{1}{2} \left[(\bar{u}^d \bar{u}_i^d)|_{x+h,y,z} + (\bar{u}^d \bar{u}_i^d)|_{x,y,z} \right] - \frac{1}{2} \left[(\bar{u}^d \bar{u}_i^d)|_{x,y,z} + (\bar{u}^d \bar{u}_i^d)|_{x-h,y,z} \right] \right\} \\ &= \frac{1}{2h} \left[(\bar{u}^d \bar{u}_i^d)|_{x+h,y,z} - (\bar{u}^d \bar{u}_i^d)|_{x-h,y,z} \right] = I \sum_{l,m,n} \sum_{p,q,r} p' \hat{G}^N(p'; h) \widehat{u}^d(p, q, r) \widehat{u}_i^d(l, m, n) e^{I(p'x + q'y + r'z)}, \quad (25) \end{aligned}$$

having defined $\hat{G}^N(\chi; h) \equiv \sin(\chi h)/(\chi h)$, whereby the superscript *N* highlights the numerical character of this 1D transfer function. As is well known, formula (25) is exactly equivalent to that obtainable by discretizing the continuous convective term in the divergence form (9), i.e. $\partial_x(\bar{u} \bar{u}_i)$, in a central second order FD-manner. As highlighted above, this aspect leads some authors to consider FD-based methods able to induce top-hat filtering. In actual fact, it is easy to deduce that the mean value formula is not able to induce any numerical filter, letting the shape of the transfer function to be governed by the flux reconstruction.

Similarly, one generalizes the (25) for expressing the other convective fluxes along *y*- and *z*-directions, respectively,

$$NSF_{c,ij}^d = I \sum_{l,m,n} \sum_{p,q,r} p'_j \hat{G}^N(p'_j; h) \widehat{u}_j^d(p, q, r) \widehat{u}_i^d(l, m, n) e^{I \sum_{k=1}^3 p'_k x_k}. \quad (26)$$

The diffusive flux is discretized at second order accuracy on a centered stencil as

$$\begin{aligned} \left(\frac{\delta}{\delta x} \left(v \frac{\delta \bar{u}_i^d}{\delta x} \right) \right)_{NSF} &\triangleq NSF_{d,i1}^d = \frac{v}{h^3} \left[\left(\frac{\delta \bar{u}_i^d}{\delta x} \right)|_{x+h/2,y,z} h^2 - \left(\frac{\delta \bar{u}_i^d}{\delta x} \right)|_{x-h/2,y,z} h^2 \right] \\ &= \frac{v}{h} \left[\left(\frac{\bar{u}_i^d|_{x+h,y,z} - \bar{u}_i^d|_{x,y,z}}{h} \right) - \left(\frac{\bar{u}_i^d|_{x,y,z} - \bar{u}_i^d|_{x-h,y,z}}{h} \right) \right] \\ &= v \left(\frac{\bar{u}_i^d|_{x+h,y,z} - 2\bar{u}_i^d|_{x,y,z} + \bar{u}_i^d|_{x-h,y,z}}{h^2} \right) = -v \sum_{l,m,n} l^2 \hat{D}^N(l; h) \widehat{u}_i^d(l, m, n) e^{I(lx + my + nz)}, \quad (27) \end{aligned}$$

where the numerical transfer function $\hat{D}^N(\chi; h) \equiv 2[1 - \cos(\chi h)]/(\chi h)^2$ has been introduced. Accordingly, (27) is generalized to express the other convective fluxes along *y*- and *z*-directions

$$NSF_{d,ij}^d = -v \sum_{l,m,n} l_j^2 \hat{D}^N(l_j; h) \widehat{u}_i^d(l, m, n) e^{I \sum_{k=1}^3 l_k x_k}. \quad (28)$$

Hence, according to (10), (26) and (28), one the *NSF*^{II}-based discrete equation for the *i*th velocity component can be written

$$\begin{aligned} \left(\frac{\partial \bar{u}_i^d}{\partial t} \right)_{NSF^{II}} &= - \sum_{j=1}^3 \left(NSF_{c,ij}^d + NSF_{d,ij}^d \right) \\ &= -I \sum_{l,m,n} \sum_{p,q,r} \left[\sum_{j=1}^3 p'_j \hat{G}^N(p'_j; h) \widehat{u}_j^d(p, q, r) \right] \widehat{u}_i^d(l, m, n) e^{I \sum_{k=1}^3 p'_k x_k} - v \sum_{l,m,n} \sum_{j=1}^3 l_j^2 \hat{D}^N(l_j; h) \widehat{u}_i^d(l, m, n) e^{I \sum_{k=1}^3 l_k x_k}. \quad (29) \end{aligned}$$

Since using a linear interpolation for the convective flux, which is a quadratic function, cannot be assumed to be a congruent approximation, the second option that can be considered for the central-based discretization is now illustrated. In fact, each velocity component can be interpolated linearly and the quadratic product can then be constructed. A depth analysis of these

choices is reported in Ref. [21]. This scheme will be denoted as NSV (Non-Staggered Velocity) reconstruction. After some manipulations, the following expression results

$$\begin{aligned} \left(\frac{\partial(\bar{u}^d \bar{u}_i^d)}{\partial x} \right)_{NSV} &\triangleq NSV_{c,i1}^II = \frac{1}{h^3} \left(\bar{u}^d|_{x+h/2,y,z} \bar{u}_i^d|_{x+h/2,y,z} h^2 - \bar{u}^d|_{x-h/2,y,z} \bar{u}_i^d|_{x-h/2,y,z} h^2 \right) \\ &= \frac{1}{h} \left(\frac{\bar{u}^d|_{x+h,y,z} + \bar{u}^d|_{x,y,z}}{2} \frac{\bar{u}_i^d|_{x+h,y,z} + \bar{u}_i^d|_{x,y,z}}{2} - \frac{\bar{u}^d|_{x-h,y,z} + \bar{u}^d|_{x,y,z}}{2} \frac{\bar{u}_i^d|_{x-h,y,z} + \bar{u}_i^d|_{x,y,z}}{2} \right) \\ &= \frac{1}{2} NSF_{c,i1}^II + \frac{1}{4h} \left[\bar{u}^d|_{x,y,z} \left(\bar{u}_i^d|_{x+h,y,z} - \bar{u}_i^d|_{x-h,y,z} \right) + \bar{u}_i^d|_{x,y,z} \left(\bar{u}^d|_{x+h,y,z} - \bar{u}^d|_{x-h,y,z} \right) \right] \\ &= I \sum_{l,m,n} \sum_{p,q,r} \frac{p'}{2} \left\{ \widehat{G}^N(p'; h) + \widehat{G}(p'; h) \cos \left[\left(\frac{p'}{2} - l \right) h \right] \right\} \widehat{u}^d(p, q, r) \widehat{u}_i^d(l, m, n) e^{I(p'x + q'y + r'z)}. \end{aligned} \quad (30)$$

Similarly, (30) is generalized to express the other convective fluxes along y- and z-directions

$$NSV_{c,ij}^II = I \sum_{l,m,n} \sum_{p,q,r} \frac{p'}{2} \left\{ \widehat{G}^N(p'; h) + \widehat{G}(p'; h) \cos \left[\left(\frac{p'}{2} - l_j \right) h \right] \right\} \widehat{u}_j^d(p, q, r) \widehat{u}_i^d(l, m, n) e^{I \sum_{k=1}^3 p'_k x_k}, \quad (31)$$

having defined $p \equiv p_1$, $q \equiv p_2$, $r \equiv p_3$, $l \equiv l_1$, $m \equiv l_2$, $n \equiv l_3$. Note the appearance of the term $\cos \left[\left(\frac{p'}{2} - l_j \right) h \right]$, implying the coupled action of the non-linear term, producing “aliased” frequencies upon the action of the transfer function \widehat{G} . Concerning the discrete diffusive flux $NSV_{d,ij}^II$, it is exactly the same as that defined by $NSF_{d,ij}^II$ in (26) owing to its linearity.

Hence, according to (10) and (31), the NSV^{II}-based discrete equation for the i th velocity component can be written

$$\begin{aligned} \left(\frac{\partial \bar{u}_i^d}{\partial t} \right)_{NSV} &= - \sum_{j=1}^3 \left(NSV_{c,ij}^II + NSV_{d,ij}^II \right) \\ &= \left(\frac{\partial \bar{u}_i^d}{\partial t} \right)_{NSF} - \frac{1}{2} NSF_{c,i1}^II - I \sum_{l,m,n} \sum_{p,q,r} \sum_{j=1}^3 \left\{ \frac{p'_j}{2} \widehat{G}(p'; h) \cos \left[\left(\frac{p'_j}{2} - l_j \right) h \right] \right\} \widehat{u}_j^d(p, q, r) \widehat{u}_i^d(l, m, n) e^{I \sum_{k=1}^3 p'_k x_k} \\ &= -I \sum_{l,m,n} \sum_{p,q,r} \left[\sum_{j=1}^3 \frac{p'_j}{2} \left\{ \widehat{G}^N(p'; h) + \widehat{G}(p'; h) \cos \left[\left(\frac{p'_j}{2} - l_j \right) h \right] \right\} \widehat{u}_j^d(p, q, r) \right] \widehat{u}_i^d(l, m, n) e^{I \sum_{k=1}^3 p'_k x_k} \\ &\quad - \nu \sum_{l,m,n} \sum_{j=1}^3 l_j^2 \widehat{D}^N(l_j; h) \widehat{u}_i^d(l, m, n) e^{I \sum_{k=1}^3 l_k x_k}. \end{aligned} \quad (32)$$

The induced numerical transfer functions (26) and (31), corresponding to the two discretizations $NSF_{c,ij}^II$ and $NSV_{c,ij}^II$, are plotted versus the exact one $\widehat{G}_x(p', q' = p', r' = p'; \Delta_{eff}) = [\sin(\xi Q/2)/(\xi Q/2)]^3$, for both $Q = 1$ and $Q = 2$, in Figs. 3(a) and (b). For graphical reasons, a 1D section is plotted fixing $p' = q' = r'$ for $0 \leq p'h = \xi \leq \pi$. In the expression of $NSV_{c,ij}^II$ there is the isolate presence of the wavenumber l outside the sum $p' = (p + l)$ and it is therefore used as a plotting parameter. From a comparison between the exact and the numerical three-dimensional transfer functions, it appears that the value $Q = 1$ accords better than $Q = 2$ and this fact somehow contradicts the $Q = 2$ value expected from the classical 1D analysis. Furthermore, the numerical transfer function \widehat{D} in Eq. (28), induced by the discretization of the diffusive fluxes (which is the same for both $NSF_{d,ij}^II$ and $NSV_{d,ij}^II$), is similarly plotted in Fig. 3(g). The agreement appears more satisfactory for the value $Q = 1$ also in this case. Now the curve overestimates the exact one a fact that gives an indication that the second order discretization of the diffusive flux induces implicitly a numerical filter that is quite different from the top-hat one. Before analyzing the differences in greater depth, let us now address the counterpart of these FV discretizations in the case of a staggered collocation of the velocity components.

3.3.2. A second order accurate central reconstruction on staggered grids

Let us now consider a classical staggered collocation of the velocity components, which is defined according to the requirements of an Exact Projection Method (EPM) for solving the Navier–Stokes equations governing an incompressible flow. Indeed, staggering the velocity components in a second order accurate method allows the divergence-free velocity constraint to be accomplished, in a discrete sense, up to machine-precision. This method is also traditionally referred to as the MAC method [12,15,26,40]. This scheme will be denoted as SV (Staggered Velocity) discretization. Because of the staggering, the application of the mean value integration formula requires transversal interpolation of the velocity components for the evaluation of the convective flux on the mid-points. Note that both formulas NSF_c and NSV_c , previously deduced for the non-staggered grid, could still be used even for staggered collocation, provided that $i = j$. In fact, when $i \neq j$, exploiting a flux-based interpolation (i.e. the NSF_c scheme) is not practicable on staggered grids and the velocity components require interpolation

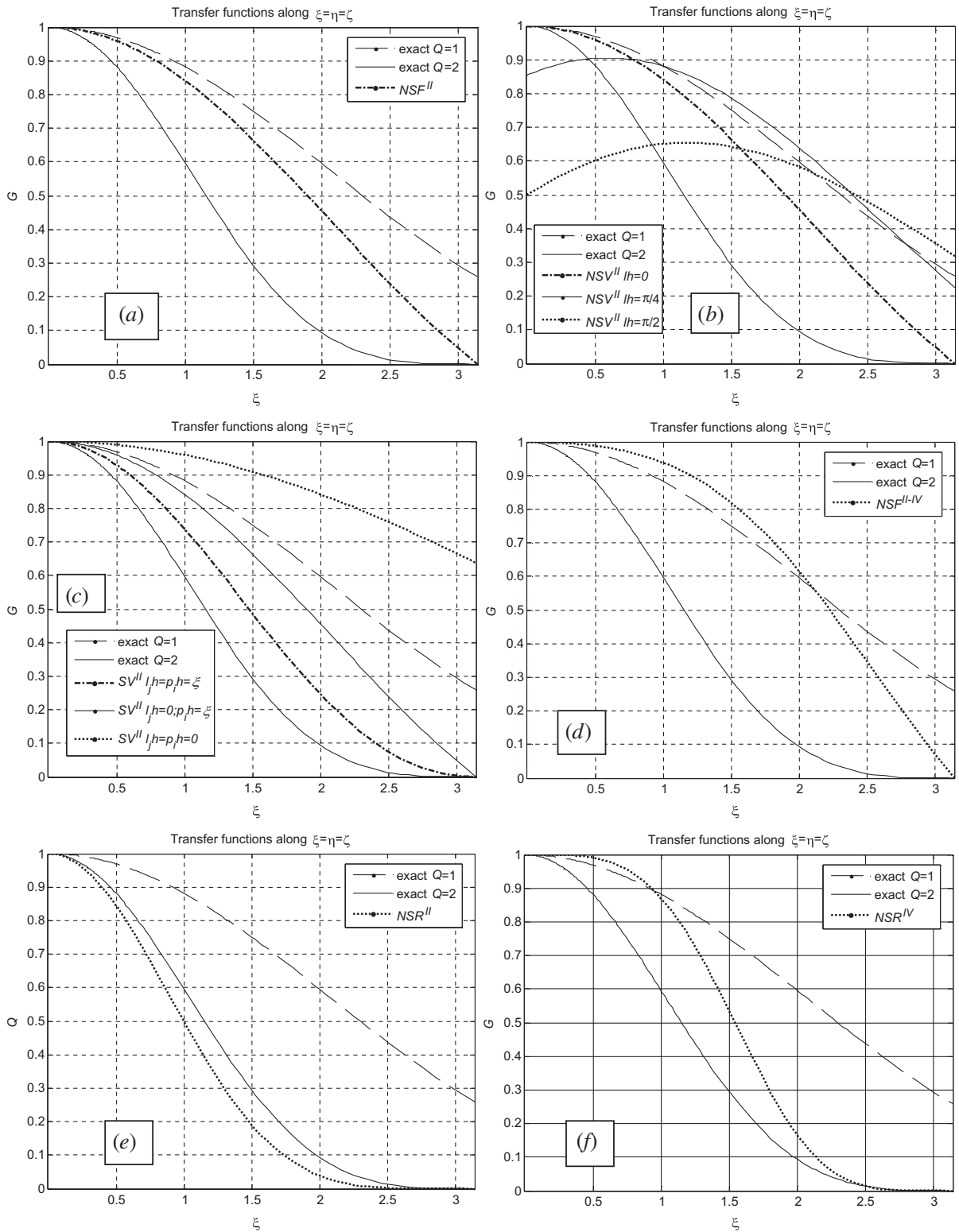


Fig. 3a–f. Implicit transfer functions induced by the FV-based discretization of the convective term plotted versus the analytical one \hat{G}_x for $Q=1$ (dot line) and 2 (continuous line), by defining $\xi = p/h$, $\eta = q/h$, $\zeta = r/h$ and forcing the constraint $0 \leq \xi = \eta = \zeta \leq \pi$.

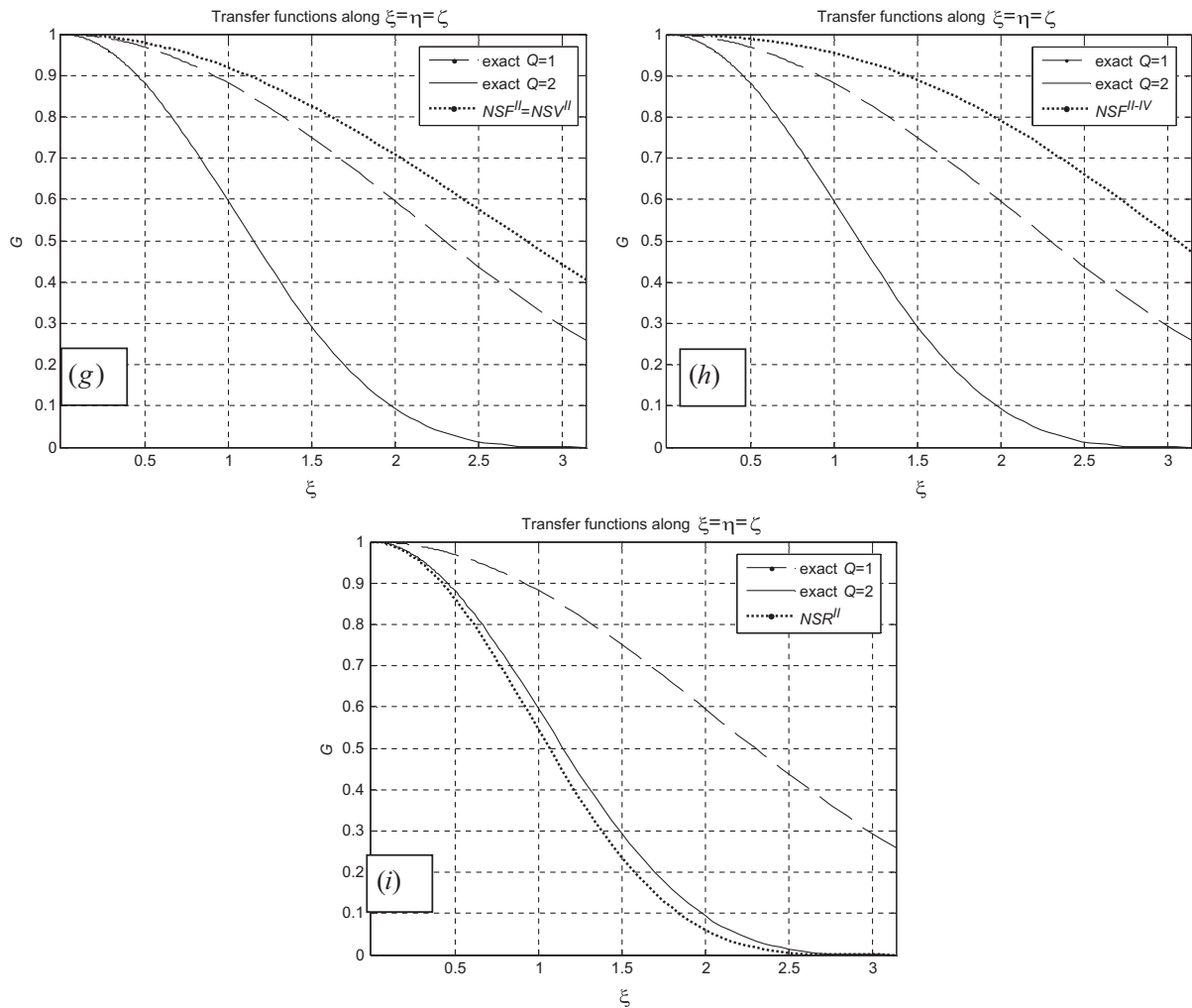


Fig. 3g–i. Implicit transfer functions induced by the FV-based discretization of the diffusive term plotted versus the analytical one \hat{G}_x for $Q = 1$ (dot line) and 2 (continuous line), by defining $\xi = p'h$, $\eta = q'h$, $\zeta = r'h$ and forcing the constraint $0 \leq \xi = \eta = \zeta \leq \pi$. Note that (g) is the same for NSF, NSV and SV reconstructions, too.

on different stencils. Therefore, the previous formula (31) is exclusively exploited for prescribing $SV_{c,11}^{II} = NSV_{c,11}^{II}$, $SV_{c,22}^{II} = NSV_{c,22}^{II}$, $SV_{c,33}^{II} = NSV_{c,33}^{II}$, the formulas for the other directions now being deduced.

The effect of the staggering is in fact clearly highlighted by evaluating the expressions of the formula for the cross-component convective fluxes. For example, considering flux vu (that is $i = 1, j = 2$), after some manipulations the formula is written

$$\begin{aligned}
 \left(\frac{\delta(\bar{v}^d \bar{u}^d)}{\delta y} \right)_{SV} &\triangleq SV_{c,12}^{II} = \frac{1}{h^3} \left[\left(\bar{v}^d|_{x,y+h/2,z} \bar{u}^d|_{x,y+h/2,z} \right) h^2 - \left(\bar{v}^d|_{x,y-h/2,z} \bar{u}^d|_{x,y-h/2,z} \right) h^2 \right] \\
 &= \frac{1}{h} \left\{ \left[\frac{1}{2} \left(\bar{v}^d|_{x+h/2,y+h/2,z} + \bar{v}^d|_{x-h/2,y+h/2,z} \right) \frac{1}{2} \left(\bar{u}^d|_{x,y+h,z} + \bar{u}^d|_{x,y,z} \right) \right] \right. \\
 &\quad \left. - \left[\frac{1}{2} \left(\bar{v}^d|_{x+h/2,y-h/2,z} + \bar{v}^d|_{x-h/2,y-h/2,z} \right) \frac{1}{2} \left(\bar{u}^d|_{x,y,z} + \bar{u}^d|_{x,y-h,z} \right) \right] \right\} \\
 &= \frac{1}{4h} \left[\left(\bar{v}^d|_{x+h/2,y+h/2,z} - \bar{v}^d|_{x+h/2,y-h/2,z} + \bar{v}^d|_{x-h/2,y+h/2,z} - \bar{v}^d|_{x-h/2,y-h/2,z} \right) \bar{u}^d|_{x,y,z} \right. \\
 &\quad \left. + \left(\bar{v}^d|_{x+h/2,y+h/2,z} + \bar{v}^d|_{x-h/2,y+h/2,z} \right) \bar{u}^d|_{x,y+h,z} - \left(\bar{v}^d|_{x+h/2,y-h/2,z} + \bar{v}^d|_{x-h/2,y-h/2,z} \right) \bar{u}^d|_{x,y-h,z} \right] \\
 &= I \sum_{l,m,n} \sum_{p,q,r} q' \left[\hat{G}(q'; h) \cos\left(\frac{ph}{2}\right) \cos\left(\frac{mh}{2}\right) \right] \hat{v}^d(p, q, r) \hat{u}^d(l, m, n) e^{I(p'x + q'y + r'z)}. \quad (33)
 \end{aligned}$$

Similarly, the evaluation of the cross-component convective flux wu (that is $i = 1, j = 3$), also allows us to write

$$\left(\frac{\delta(\overline{w^d u^d})}{\delta z} \right)_{SV} \triangleq SV_{c,13}^{II} = I \sum_{l,m,n} \sum_{p,q,r} r' \left[\widehat{G}(r'; h) \cos\left(\frac{ph}{2}\right) \cos\left(\frac{nh}{2}\right) \right] \widehat{w}^d(p, q, r) \widehat{u}^d(l, m, n) e^{I(p'x+q'y+r'z)}. \quad (34)$$

Hence, generalizing formulas (33) and (34) for any $i \neq j$ results in

$$SV_{c,ij}^{II} = I \sum_{l,m,n} \sum_{p,q,r} p'_j \left[\widehat{G}(p'_j; h) \cos\left(\frac{l_j h}{2}\right) \cos\left(\frac{p_j h}{2}\right) \right] \widehat{u}_j^d(p, q, r) \widehat{u}_i^d(l, m, n) e^{I \sum_{k=1}^3 p'_k x_k} \quad (35)$$

As far as the diffusive flux is concerned, the second order accurate discretization on a staggered grid produces no difference in the formulas already illustrated for the non-staggered case (28), $SV_{d,ij}^{II} = NSF_{d,ij}^{II} = NSV_{d,ij}^{II}$ is therefore simply considered.

According to Eqs. (10), (31) and (35), the SV^{II} -based discrete equation for the i th velocity component can be written

$$\begin{aligned} \left(\frac{\partial \widehat{u}_i^d}{\partial t} \right)_{SV} &= - \sum_{j=1}^3 (SV_{c,ij}^{II} + SV_{d,ij}^{II}) \\ &= -I \sum_{l,m,n} \sum_{p,q,r} \left\{ \sum_{j=1}^3 \frac{p'_j \delta_{ij}}{2} \left[\widehat{G}^N(p'_j; h) + \widehat{G}(p'_j; h) \cos[(p_j - l_j)h/2] \right] \right. \\ &\quad \left. + p'_j(1 - \delta_{ij}) \left[\widehat{G}(p'_j; h) \cos\left(\frac{p_j h}{2}\right) \cos\left(\frac{l_j h}{2}\right) \right] \widehat{u}_j^d(p, q, r) \right\} \widehat{u}_i^d(l, m, n) e^{I \sum_{k=1}^3 p'_k x_k} \\ &\quad - \nu \sum_{l,m,n} l_j^2 \widehat{D}^N(l_j; h) \widehat{u}_i^d(l, m, n) e^{I \sum_{k=1}^3 l_k x_k} \end{aligned} \quad (36)$$

δ_{ij} being the Kronecker symbol. Again, the appearance of the “spurious” terms $\cos(p_j h/2) \cos(l_j h/2)$ is the consequence of adopting a different collocation of the velocity. In a first approximation, wavenumbers p_i and l_j will be parameterized. The numerical transfer function in (35) is plotted in Fig. 3(c) for $0 \leq p'h = \xi \leq \pi$ versus the exact one \widehat{G}_x , while once again fixing $p' = q' = r'$ for both $Q = 1$ and $Q = 2$. The numerical transfer function for the diffusive flux was already illustrated in Fig. 3(g).

3.3.3. A hybrid second-fourth order accurate central flux reconstruction on non-staggered grid

It is well known that, in order to increase the accuracy of a FV method, both high order integration and high order interpolation of the fluxes is required (see Ref. [12]). Conversely, if the discrete integral operators $I|_{x_i-h/2}^{x_i+h/2}$ are specified at second order of accuracy, which is much more appealing than the fourth order integration, this nevertheless approaches a global second order accuracy (referred to the magnitude order of the LTE) of the FV method, regardless of any higher order accuracy of the flux reconstruction. Thus, about a question arises as to the spectral resolution gained when using a hybrid discretization, for example a fourth order accurate interpolation of the fluxes along with the second order accurate mean value formula for the integrals. In order to highlight the hybrid character of the formula, this scheme will be denoted as NSF^{II-IV} and it is obtained according to

$$\begin{aligned} \left(\frac{\delta(\overline{u^d u_i^d})}{\delta x} \right)_{NSF^{II-IV}} &\triangleq NSF_{c,i1}^{II-IV} = \frac{1}{h^3} \left\{ \left[(\overline{u^d u_i^d})|_{x+h/2,y,z} \right] h^2 - \left[(\overline{u^d u_i^d})|_{x-h/2,y,z} \right] h^2 \right\} \\ &= \frac{5}{4} NSF_{c,i1}^{II} - \frac{1}{16h} \left[(\overline{u^d u_i^d})|_{x+2h,y,z} - (\overline{u^d u_i^d})|_{x-2h,y,z} \right] \\ &= I \sum_{l,m,n} \sum_{p,q,r} p'_j \widehat{G}^N(p'_j; h) \left[\frac{5 - \cos(p'h)}{4} \right] \widehat{u}_j^d(p, q, r) \widehat{u}_i^d(l, m, n) e^{I(p'x+q'y+r'z)}. \end{aligned} \quad (37)$$

Similarly, (37) is generalized to express the other convective fluxes along y - and z -directions

$$NSF_{c,ij}^{II-IV} = I \sum_{l,m,n} \sum_{p,q,r} p'_j \widehat{G}^N(p'_j; h) \left[\frac{5 - \cos(p'h)}{4} \right] \widehat{u}_j^d(p, q, r) \widehat{u}_i^d(l, m, n) e^{I \sum_{k=1}^3 p'_k x_k}. \quad (38)$$

Regarding the discretization of the diffusive flux, a fourth order accurate formula for the derivative and the mean value formula for the integral is considered resulting in

$$\begin{aligned} \left(\frac{\delta}{\delta x} \left(v \frac{\delta \bar{u}_i^d}{\delta x} \right)^d \right)_{NSF^{II-IV}} &\triangleq NSF_{d,i1}^{II-IV} = \frac{1}{h^3} \left[\left(v \frac{\delta \bar{u}_i^d}{\delta x} \right) \Big|_{x+h/2,y,z} h^2 - \left(v \frac{\delta \bar{u}_i^d}{\delta x} \right) \Big|_{x-h/2,y,z} h^2 \right] \\ &= v \left(\frac{-\bar{u}_i^d|_{x+2h,y,z} + 28\bar{u}_i^d|_{x+h,y,z} - 54\bar{u}_i^d|_{x,y,z} + 28\bar{u}_i^d|_{x-h,y,z} - \bar{u}_i^d|_{x-2h,y,z}}{24h^2} \right) \\ &= -v \sum_{l,m,n} l^2 \left[\frac{7\hat{D}^N(l;h) - \hat{D}^N(2l;h)}{6} \right] \widehat{\bar{u}}_i^d(l,m,n) e^{l(kx+my+nz)}. \end{aligned} \quad (39)$$

The other diffusive fluxes along y - and z -directions can simply be generalized according to

$$NSF_{d,ij}^{II-IV} = -v \sum_{l,m,n} l_j^2 \left[\frac{7\hat{D}^N(l_j;h) - \hat{D}^N(2l_j;h)}{6} \right] \widehat{\bar{u}}_i^d(l,m,n) e^{l \sum_{k=1}^3 l_k x_k}. \quad (40)$$

Hence, according to (10), (38) and (40), the NSF^{II-IV} -based discrete equation for the i th velocity component can be written

$$\begin{aligned} \left(\frac{\partial \bar{u}_i^d}{\partial t} \right)_{NSF^{II-IV}} &= - \sum_{j=1}^3 \left(NSF_{c,ij}^{II-IV} + NSF_{d,ij}^{II-IV} \right) = -I \sum_{l,m,n} \sum_{p,q,r} \left\{ \sum_{j=1}^3 p_j \hat{G}^N(p'_j;h) \left[\frac{5 - \cos(p'_j h)}{4} \right] \widehat{\bar{u}}_j^d(p,q,r) \right\} \widehat{\bar{u}}_i^d(l,m,n) e^{l \sum_{k=1}^3 p'_k x_k} \\ &\quad - v \sum_{l,m,n} \sum_{j=1}^3 l_j^2 \left[\frac{7\hat{D}^N(l_j;h) - \hat{D}^N(2l_j;h)}{6} \right] \widehat{\bar{u}}_i^d(l,m,nt) e^{l \sum_{k=1}^3 l_k x_k}. \end{aligned} \quad (41)$$

The numerical transfer function in (38) is plotted in Fig. 3(d) for $0 \leq p'h = \xi \leq \pi$ versus the exact one \hat{G}_x plotted while fixing $p' = q' = r'$ for both $Q = 1$ and $Q = 2$. At first glance, despite the global second order accuracy of the method, the induced transfer function remains closer to the identity operator for a wider range of wavenumbers, the shape generally no longer appearing similar to the expected top-hat filter. This feature accords with the inability of the mean value formula to act as an implicit top-hat filter and the shape of the transfer function is governed by the fourth order flux interpolation.

Considering the transfer function induced by the discretization of the diffusive flux, Fig. 3(h) shows a similarity to Fig. 3(g), apart from a greater departure from the theoretical curve.

3.3.4. Some higher order accurate central reconstructions on a non-staggered grid

In this sub-section, the second and fourth order accurate schemes used in the LES methodology illustrated in Refs. [16,24] are analyzed since the authors addressed such discretizations as FV-based implementation, performed by using a cell-centered discretization and a trapezoidal rule for the integration of the fluxes. The integral form of the LES equation was never actually addressed but only the filtered equation in divergence form, i.e. Eq. (9), is used. Moreover, the LES were performed without supplying any explicit filtering [16]. In other words, the FD-like discrete derivative $\delta_{x_i}(\bar{u}^d \bar{u}_i^d)$ is used instead of the genuine integral-based FV counterpart $\overline{\delta_{x_i}(\bar{u}^d \bar{u}_i^d)}$. Therefore, this is an illustrative case in which the shape of the filter is implicitly induced by the discretization of the only divergence of the fluxes (22) and (24). We call these schemes *NSR* (Non-Staggered Reconstruction) since a transversal reconstruction is also used to evaluate the flux.

Specifically, the second order discretization of the convective flux, for example for the x -direction derivative, is written according to [16,24]

$$\begin{aligned} \left(\frac{\delta(\bar{u}^d \bar{u}_i^d)}{\delta x} \right)_{NSR^{II}} &\triangleq NSR_{c,i1}^{II} = \frac{1}{2h} (r|_{x+h,y,z} - r|_{x-h,y,z}), \\ r|_{x,y,z} &= \frac{s|_{x,y,z}}{2} + \frac{s|_{x,y+h,z} + s|_{x,y-h,z}}{4}, \\ s|_{x,y,z} &= \frac{1}{2} (\bar{u}^d \bar{u}_i^d)|_{x,y,z} + \frac{(\bar{u}^d \bar{u}_i^d)|_{x,y,z+h} + (\bar{u}^d \bar{u}_i^d)|_{x,y,z-h}}{4}, \end{aligned} \quad (42)$$

which represents a second order accurate derivative based on an average along the $y - z$ surface of area $2h \times 2h$ (see Ref. [16]). While denoting for the sake of simplicity $\bar{u}^d \bar{u}_i^d = f$, formula (42) can be expanded and, after some manipulation, the induced transfer function can be expressed as

$$\begin{aligned}
NSR_{c,11}^{II} = & \frac{1}{32h} \{ [4f_{x+h,y,z} + 2(f_{x+h,y,z+h} + f_{x+h,y,z-h} + f_{x+h,y+h,z} + f_{x+h,y-h,z}) + f_{x+h,y+h,z+h} + f_{x+h,y+h,z-h} + f_{x+h,y-h,z+h} \\
& + f_{x+h,y-h,z-h}] - [4f_{x-h,y,z} + 2(f_{x-h,y,z+h} + f_{x-h,y,z-h} + f_{x-h,y+h,z} + f_{x-h,y-h,z}) + f_{x-h,y+h,z+h} + f_{x-h,y+h,z-h} \\
& + f_{x-h,y-h,z+h} + f_{x-h,y-h,z-h}] \} \\
= & I \sum_{l,m,n} \sum_{p,q,r} p' \left\{ \frac{\widehat{G}^N(p'; h)}{4} [1 + \cos(q'h)] [1 + \cos(r'h)] \right\} \widehat{u}^d(p, q, r) \widehat{u}_i^d(l, m, n) e^{I(p'x + q'y + r'z)}. \quad (43)
\end{aligned}$$

Note that the computational stencil has no involved nodes on the plane at the x position. Similarly, one works for the derivatives of the other convective fluxes along y - and z -directions, respectively so that the extension of (43) allows us to rewrite the formula in the generic directions

$$NSR_{c,ij}^{II} = I \sum_{l,m,n} \sum_{p,q,r} p'_j \left\{ \frac{\widehat{G}^N(p'_j; h)}{4} \prod_{k=1, k \neq j}^3 [1 + \cos(p'_k h)] \right\} \widehat{u}_j^d(p, q, r) \widehat{u}_i^d(l, m, n) e^{I \sum_{k=1}^3 p'_k x_k} \quad (44)$$

With regard to the discretization of the diffusive term, the scheme is obtained by means of two consecutive applications of the first derivatives (see Ref. [16]). In practical terms, a sequential application of “inner” and “outer” derivatives leads [16] to the total formula (note that the position $\widehat{u}_i^d = f$ is used here)

$$\begin{aligned}
\left(\frac{\partial}{\partial x} \left[v \frac{\partial (\widehat{u}_i^d)}{\partial x} \right] \right)_{NSR^{II}} & \triangleq NSR_{d,11}^{II} = \frac{v}{16h^2} [f_{x+h,y-h,z-h} + f_{x-h,y-h,z+h} + f_{x-h,y-h,z-h} + f_{x+h,y+h,z+h} + f_{x-h,y+h,z-h} + f_{x-h,y+h,z+h} \\
& + f_{x+h,y-h,z+h} + f_{x+h,y+h,z-h} + 2(f_{x-h,y,z-h} + f_{x-h,y-h,z} + f_{x-h,y+h,z} + f_{x-h,y,z+h} + f_{x+h,y+h,z} \\
& + f_{x+h,y,z+h} + f_{x+h,y-h,z} + f_{x+h,y,z-h} - f_{x,y+h,z+h} - f_{x,y-h,z-h} - f_{x,y-h,z+h} \\
& - f_{x,y+h,z-h}) + 4(f_{x+h,y,z} + f_{x-h,y,z} - f_{x,y+h,z} - f_{x,y-h,z} - f_{x,y,z+h} - f_{x,y,z-h}) - 8f_{x,y,z}] \\
= & -v \sum_{l,m,n} l^2 \frac{\widehat{D}^N(k; h) [\cos(mh) + 1] [\cos(nh) + 1]}{4} \widehat{u}_i^d(l, m, n) e^{I(lx + my + nz)}. \quad (45)
\end{aligned}$$

Subsequently, the other diffusive fluxes along y - and z -directions can be generalized according to

$$NSR_{d,ij}^{II} = -v \sum_{l,m,n} l_j^2 \left[\frac{\widehat{D}^N(l_j; h)}{4} \prod_{k=1, k \neq j}^3 [1 + \cos(l_k h)] \right] \widehat{u}_i^d(l, m, n) e^{I \sum_{k=1}^3 l_k x_k}. \quad (46)$$

Hence, the NSR^{II} -based discrete equation for the i th velocity component can be written according to

$$\begin{aligned}
\left(\frac{\partial \widehat{u}_i^d}{\partial t} \right)_{NSR^{II}} & = - \sum_{j=1}^3 (NSR_{c,ij}^{II} + NSR_{d,ij}^{II}) = -I \sum_{l,m,n} \sum_{p,q,r} \left\{ \sum_{j=1}^3 p'_j \left\{ \frac{\widehat{G}^N(p'_j; h)}{4} \prod_{k=1, k \neq j}^3 [1 + \cos(p'_k h)] \right\} \widehat{u}_j^d(p, q, r) \right\} \widehat{u}_i^d(l, m, n) e^{I \sum_{k=1}^3 p'_k x_k} \\
& - v \sum_{l,m,n} \sum_{j=1}^3 l_j^2 \left[\frac{\widehat{D}^N(l_j; h)}{4} \prod_{k=1, k \neq j}^3 [1 + \cos(l_k h)] \right] \widehat{u}_i^d(l, m, n) e^{I \sum_{k=1}^3 l_k x_k}. \quad (47)
\end{aligned}$$

Let us now address the fourth-order accurate discretization in Refs. [16,24]. The scheme uses an additional fourth-order accurate interpolation, applied in directions perpendicular to the direction with respect to that which the derivative is evaluated. As stated for the second-order scheme, the authors claim that this procedure increases robustness, while the formal fourth-order of the scheme is preserved. The fourth-order scheme for the convective term is rewritten here according to

$$\begin{aligned}
\left(\frac{\partial (\widehat{u}_i^d \widehat{u}_i^d)}{\partial x} \right)_{NSR^{IV}} & \triangleq NSR_{c,11}^{IV} = \frac{4}{3} \left(\frac{r|_{x+h,y,z} - r|_{x-h,y,z}}{2h} \right) - \frac{1}{3} \left(\frac{r|_{x+2h,y,z} - r|_{x-2h,y,z}}{4h} \right); \\
r|_{x,y,z} & = \frac{5}{8} s|_{x,y,z} + \frac{1}{2} \frac{s|_{x,y+h,z} + s|_{x,y-h,z}}{2} - \frac{1}{8} \frac{s|_{x,y+2h,z} + s|_{x,y-2h,z}}{2}, \\
s|_{x,y,z} & = \frac{5}{8} (\widehat{u}^d \widehat{u}_i^d)|_{x,y,z} + \frac{(\widehat{u}^d \widehat{u}_i^d)|_{x,y,z+h} + (\widehat{u}^d \widehat{u}_i^d)|_{x,y,z-h}}{4} - \frac{(\widehat{u}^d \widehat{u}_i^d)|_{x,y,z+2h} + (\widehat{u}^d \widehat{u}_i^d)|_{x,y,z-2h}}{16} \quad (48)
\end{aligned}$$

and the resulting computational stencil extends over a $5 \times 5 \times 5$ computational molecule around the center (x, y, z) . However, only 100 non-vanishing coefficients are in effect. For the sake of brevity, the full formula is not reported here. When rewriting formula (48) for the derivatives of the other convective fluxes along y - and z -directions, in terms of the wavenumber components, we have

$$NSR_{c,ij}^{IV} = I \sum_{l,m,n} \sum_{p,q,r} p_j' \left\{ \widehat{G}^N(p_j'; h) 3 \left[4 - \cos(p_j' h) \right] \prod_{k=1, k \neq j}^3 c_k \right\} \widehat{u}_j^d(p, q, r) \widehat{u}_i^d(l, m, n) e^{I \sum_{k=1}^3 p_k' x_k},$$

$$c_k = \frac{\cos(p_k' h)}{6} \left[\frac{\cos(p_k' h)}{2} - 1 \right] - \frac{1}{4}. \quad (49)$$

The fourth order accurate discretization of the viscous term is obtained by means of a sequential combination of two fourth-order accurate derivatives. The first derivative is prescribed in the staggered location, leading to a 64-node stencil. The second derivative, centered on the FV, follows as a similar application developed for the second order scheme [16]. For the sake of brevity, such a discretization of the viscous term is not analyzed. By means of (10) and (49) it will then be a simple task to write the NSR^{IV} -based discrete equation for the i th velocity component.

The resulting implicit transfer functions in (44), (46) and (49) are plotted in Fig. 3(e), (i) and (f), respectively, versus the analytical one for $Q = 1$ and $Q = 2$, by defining $\xi = p'h$, $\eta = q'h$, $\zeta = r'h$ and forcing the constraint $0 \leq \xi = \eta = \zeta \leq \pi$. The appearance of some specific features of such curves will be discussed in detail in the discussion.

3.4. The differences between differential and integral-based approaches. Discussion

In order to clarify the differences between the genuine integral-based FV approach and the FD-based discretization of the divergence form, the analysis reported in Ref. [24], is now used as a guideline.

The (1D) filtered Burgers equation, was written in differential divergence form [24], that is $\partial_t \bar{u} + \frac{1}{2} \partial_x \bar{u}^2 = 0$ (commutation property is therefore needed), \bar{u} being supposed to be the top-hat filtered velocity. After introducing a discrete differential operator δ_x , according to Ref. [24], the discrete derivative of a sampled function “can be expressed as $\delta_x f = \partial_x \hat{f}$, where \hat{f} denotes the filtering of f with the numerically induced filter (\cdot) ”. The semi-discretized equation was then rewritten explicitly in terms of the numerically induced resolved flux, that is $\partial_t \bar{u} + \frac{1}{2} \partial_x \bar{u}^2 + \frac{1}{2} \partial_x (\bar{u}^2 - \hat{u}^2) = 0$. Finally, a finite differencing formula $\delta_x^{(-n,m)} f$ (n, m being the grid limits of the stencil) can be organized in such a way that the “total induced numerical filter can hence be expressed as a weighted average of skewed top-hat filters”. The clue in the analysis described in Ref. [24] is that using a discrete derivative of the flux $\delta_x^{(-n,m)} f$ induces the continuous derivative of the filtered flux, that is $\partial_x [L_{-n,m}(f)] = \partial_x \hat{f}$ (the numerical filter is denoted in general with \hat{f} without specifying the stencil). According to such a description, an insight into FV and FD-based implicit filtering is now addressed.

In the absence of any explicit filtering, the true shape of the induced transfer function is governed only by the type of discretization of the resolved filtered flux, but a generic discretization $\delta_x^{(-n,m)} f$ does not necessarily induce the top-hat filtered time-derivative $\partial_t \bar{u}$. In order for this uncertainty to be taken into account, according to the same symbolism \hat{f} , the generic induced filtered time derivative $\partial_t \hat{u}$ is introduced. Hence, unlike the questions addressed in Ref. [24], here a generic discrete operator induces a generic filter, such that the continuous filtered equation $\partial_t \bar{u} + \frac{1}{2} \partial_x \bar{u}^2 + \frac{1}{2} \partial_x \tau = 0$ is assumed. Then, to assess if such a differential filtered equation were be equivalent to the integral-based conservation law $\partial_t \bar{u} + \frac{1}{2} \partial_x \bar{u}^2 + \frac{1}{2} \partial_x (\bar{u}^2 - \hat{u}^2) = 0$, it is necessary to fulfill two conditions: (1) a finite differencing formula $\delta_x^{(-n,m)} f$ for which the equivalence $\delta_x^{(-n,m)} f = \partial_x \hat{f} = \partial_x \bar{f}$ is induced; (2) the accomplishment of the commutation property $\partial_x (\cdot) = \partial_x (\cdot)$. The latter condition is clearly fulfilled for any uniform grid but the fulfillment of condition 1 depends on the type of scheme. For example, condition 1 is exactly verified by the classical second order finite difference $\delta_x^{(-1,1)} f = (f_{+1} - f_{-1})/2h$, since it is well known to induce the top-hat filtering $\partial_x [L_{-1,1}(f)] = \partial_x \int_{x-\Delta_{-1,1}/2}^{x+\Delta_{-1,1}/2} \frac{f(x')}{\Delta_{-1,1}} dx'$ of characteristic width $\Delta_{-1,1} = 2h$. The value of the sub-filter resolution parameter $Q = 2$ is consequently¹¹ achieved. However, the framework becomes very different when considering higher order approximations.

Following Ref. [24], the fourth order accurate central finite difference $\delta_x^{(-2,2)} f$ induces a filtered flux $\partial_x [L_{-2,2}(f)] = \partial_x \left[\frac{4}{3} \int_{x-h}^{x+h} \frac{f(x')}{2h} dx' - \frac{1}{3} \int_{x-2h}^{x+2h} \frac{f(x')}{4h} dx' \right] = \partial_x \left[\frac{4}{3} \bar{f}^{2h} - \frac{1}{3} \bar{f}^{4h} \right]$, which is, therefore, a linear combination of two local averaged functions \bar{f} over different widths. Consequently, this FD-based formula would fulfill the integral conservation law, written for a volume of linear width $\Delta_{-2,2} = Qh$, provided that the expression $(\frac{4}{3} \bar{f}^{2h} - \frac{1}{3} \bar{f}^{4h}) = \int_{x-\Delta_{-2,2}/2}^{x+\Delta_{-2,2}/2} \frac{f(x')}{\Delta_{-2,2}} dx'$ is satisfied. In terms of the top-hat transfer functions, the previous relation can be written as $\left[\frac{4}{3} \frac{\sin(kh)}{kh} - \frac{1}{3} \frac{\sin(2kh)}{2kh} \right] = \left[\frac{\sin(k\Delta_{-2,2}/2)}{k\Delta_{-2,2}/2} \right]$. The same reasoning can be also applied to the sixth-order accurate finite difference $\delta_x^{(-3,3)} f$ which results in $\partial_x [L_{-3,3}(f)] = \partial_x (\frac{2}{3} \bar{f}^{2h} - \frac{2}{3} \bar{f}^{4h} + \frac{1}{10} \bar{f}^{6h})$. Therefore, the sixth-order FD-based formula would fulfill the integral conservation law, written for a volume of linear width $\Delta_{-3,3} = Qh$, provided that the expression $(\frac{2}{3} \bar{f}^{2h} - \frac{2}{3} \bar{f}^{4h} + \frac{1}{10} \bar{f}^{6h}) = \int_{x-\Delta_{-3,3}/2}^{x+\Delta_{-3,3}/2} \frac{f(x')}{\Delta_{-3,3}} dx'$ is satisfied. In terms of the top-hat transfer

¹¹ Let us remember that, on a computational grid, the top-hat transfer function is always truncated at the Nyquist frequency and is, therefore, always an approximation of the continuous one.

functions, the expression $\left[\frac{3}{2} \frac{\sin(kh)}{kh} - \frac{3}{5} \frac{\sin(2kh)}{2kh} + \frac{1}{10} \frac{\sin(3kh)}{3kh}\right] = \left[\frac{\sin(k\Delta_{-3,3/2})}{k\Delta_{-3,3/2}}\right]$ should be satisfied. Hence, for both expressions, the ratio of LHS to RHS, say $C = C(kh; Q)$, should be equal to 1 for all resolved wavenumbers. An inspection of the plots of C , reported in Fig. 3(l) and (m) for several values of Q , shows that such equivalence is achieved only at low wavenumbers, after which there is a strong departure. What is more, increasing from fourth to sixth the accuracy order of the formula does not improve the agreement. The effective induced filter widths were estimated in Ref. [24] as $\Delta_{-2,2} = 36h/25 = 1.44h$ and $\Delta_{-3,3} = 300h/239 = 1.2552h$, but there is a clear evidence from pictures that they do not produce a good approximation of the integral conservation law.

On the opposite side, let us now consider a genuine FV-based flux reconstruction such as, for example, the fourth-order accurate formula NSF , resulting from (37). It can be shown that the linear combination of local average functions $(\bar{\delta}_x \bar{f}^d)_{NSF} = \partial_x (\frac{5}{4} \bar{f}^{2h} - \frac{1}{4} \bar{f}^{4h})$ is induced. As addressed before, the condition of equivalence to an integral conservation law over a volume of linear width $\Delta_{NSF} = Qh$ requires $\frac{5}{4} \bar{f}^{2h} - \frac{1}{4} \bar{f}^{4h} = \int_{x-\Delta_{NSF}/2}^{x+\Delta_{NSF}/2} \frac{f(x')}{\Delta_{NSF}} dx'$. In terms of the transfer functions, one has $\left[\frac{5}{4} \frac{\sin(kh)}{kh} - \frac{1}{4} \frac{\sin(2kh)}{2kh}\right] = \left[\frac{\sin(k\Delta_{NSF}/2)}{k\Delta_{NSF}/2}\right]$. Now, an inspection of the plots of C , reported in Fig. 3(n) for several values of Q shows that $C = 1$ is achieved for a wider range of resolved wavenumbers (and $1.25 \leq Q \leq 1.5$) than that obtained with the sixth-order FD scheme. Unlike the FD formulas, increasing the accuracy order of the FV-based flux reconstruction would further improve the agreement to the integral conservation law. As a matter of fact, a corroboration is in the statement of Ref. [24]: “the filter corresponding to higher-order spatial discretization is itself a higher-order filter; with increasing order, the Fourier transform of the kernel is seen to stay closer to the identity operator for a wide range of wave numbers”. This statement is consistent with the fact that a high order FD formula $\delta_x^{(-n,m)} f$ induces a filter tending towards the spectral cut-off, not to that of the top-hat. Only genuine integral-based high-order discretizations improve the approximation of the top-hat filter. Therefore, a more general link between FD and FV can be recognized by means of an approximate deconvolution operator [1,13,14] such that $[A_x^{(-n,m)}]^{-1} \bar{u} = \hat{u}$. The extension of the analysis to the 3D formulas now highlights more discrepancies between FD and FV scheme.

With regard to the discretization of the convective terms, the behavior of the 3D transfer functions induced by the NSF and NSV schemes are depicted in Fig. 3(a) and (b), respectively. As can easily be verified by inspection of (25) and (30), both become clearly coincident for $lh = 0$ (that means $\xi = p'h = ph$). In the expression of the transfer function NSV , wavenumber l remains outside the sum $p' = (p + l)$ and is therefore used as a plotting parameter. In both figures, the curves stay close to that of the exact top-hat at $Q = 1$, this fact somehow contradicting the expected accordance with $Q = 2$, as is known from the classical 1D analysis [1,5,6]. However, for non-vanishing values lh (that is $0 < \xi - ph \leq \pi/2$), the NSV produces spurious frequencies inherent to the appearance of aliasing terms (and triadic-interaction appearing from the non-linear terms, see Ref. [1]). An in-depth analysis of the aliasing errors, either in flux or in velocity interpolation, is addressed in Ref. [21]. Considering now the effect of the staggering, the transfer function induced by the second order accurate SV scheme (35) is plotted in Fig. 3(c). Owing to the staggered collocation, there is the appearance of other wavenumbers that remain outside the sums p', q', r' . Moreover, on one side SV and NSF are coincident when $l'h = 0, p'h = \xi$ (see Fig. 3(a)) and, on the other side SV and NSV are coincident for $lh=0$ (see Fig. 3(b)). In addition, when $l'h = p'h = \xi$, the curve SV tends to stay close to the exact transfer function curve at $Q = 2$, while the curve $Q = 1$ for $l'h = p'h = 0$ become largely overestimated. Such effects are a manifestation of the supplementary transversal interpolations of the velocity product, required by the staggering, that enlarges the computational stencil.

Furthermore, both the NSF^{II-IV} and the two NSR schemes are characterized by transfer functions depending exclusively on the sums p', q', r' . This confirms the fact that using the product of velocity polynomials causes the appearance of “spurious” wavenumbers. The curve of the NSR^{II} scheme in Fig. 3(e) shows a good approximation of the exact top-hat filter for the value $Q = 2$. The accuracy order is the same as that of NSF^{II} but the distinguishing fact of NSR^{II} can be addressed in the use of the trapezoidal rule associated with the transverse second order accurate multidimensional interpolation. This results in a more isotropic resolution of the built-in transfer function with respect to the wavenumbers p', q', r' . What is common in both the NSF^{II-IV} and NSR^{IV} schemes is that they are built in such a way that the accuracy order is increased only for the interpolation of the flux, and not for the discretization of the integrals. Consequently, one can see from the respective plots that a better approximation of the sharp cut-off filter at low wavenumbers, but not of the exact top-hat filter, is achieved. Interestingly, when compared to the exact transfer function at $Q = 1$, both plots in Fig. 3(d) and (f) show an overestimation of the spectral content at low wavenumbers whereas Fig. 3(e) describes a slight underestimation of the exact case for $Q = 2$. Namely, despite the fact that the NSR^{IV} formula was addressed as one of “finite-volume” [16,24], it has to be considered a high order FD-based discretization of the divergence form, because there is no associated fourth order surface integration [12]. Fig. 3(f) seems indicative of the fact that the shape of the transfer function actually seems like a “deconvolution-based” counterpart of that of the top-hat.

With regard to the discretization of the diffusive terms, the transfer functions induced by the FV-based schemes are shown in Fig. 3(g)–(i). The linearity of the term naturally produces some simplification in the resulting curves. The same comments addressed above to the discretization of the convective term can generally be applied. Mainly, the NSR^{II} scheme is the only one characterized by good agreement with the $Q = 2$ value. It is worthwhile remembering that the SGS term, when modeled according to the eddy viscosity assumption, turns out to be discretized according to the previous diffusive flux formulas.

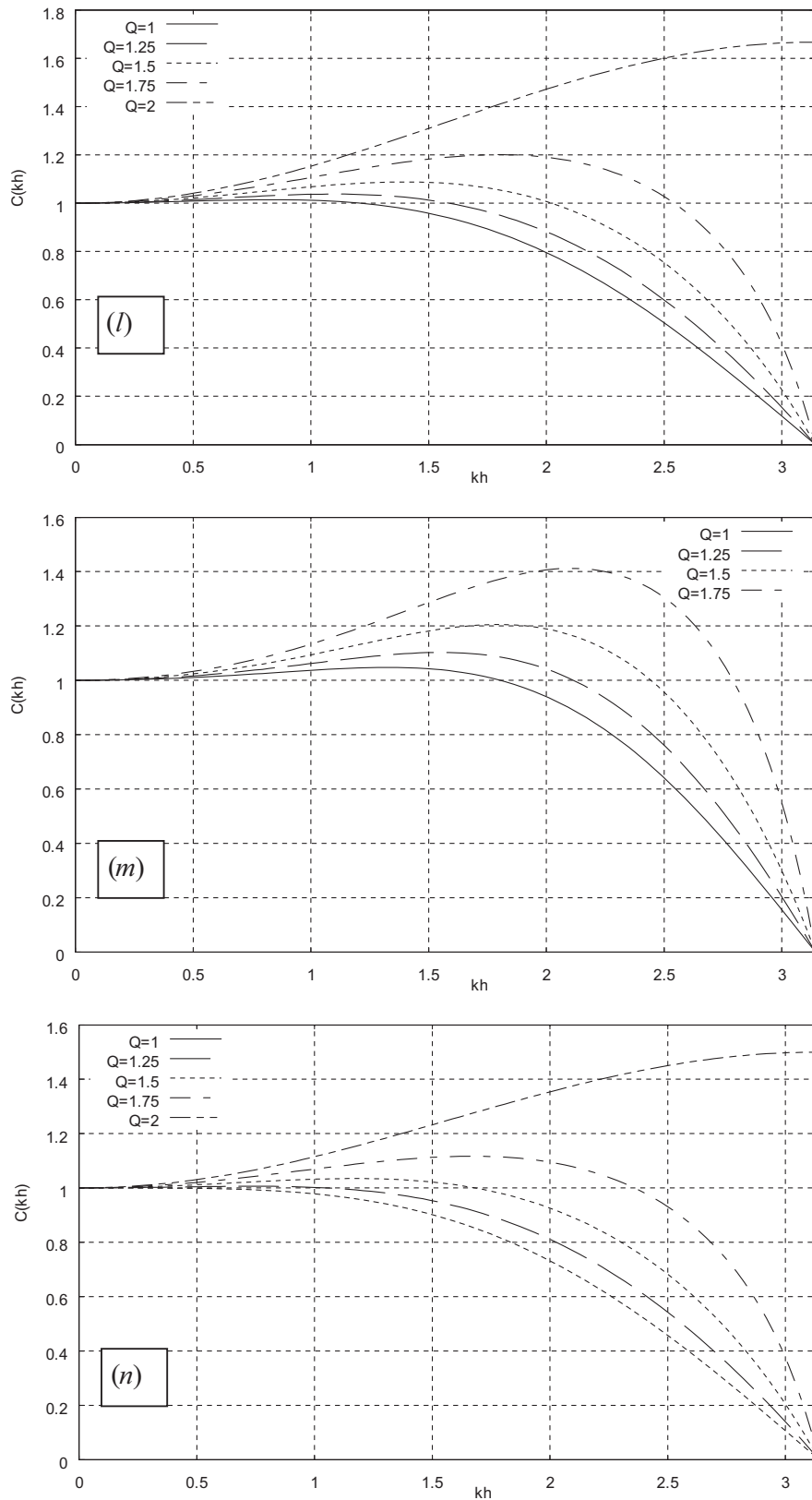


Fig. 31–n. Plots of the ratio between the numerically induced transfer functions and that one corresponding to the integral conservation law for various values of Q ; (l) fourth-order and (m) sixth-order FD-based schemes, (n) fourth-order FV-based scheme.

3.5. Some brief quantitative results on the filtering errors analysis

Quantitative analyses of the effective filter width and shape have been the object of some studies see Refs. [1,4,6,24], which have exploited some one-dimensional estimations that in order to characterize the filter kernel. However, the results appear rather controversial. Here, the goal is not to assess the validity of these proposals but simply to illustrate the results obtained from their application. Thus, in order to evaluate the built-in filter width, three different criteria are used: (a) the 1/2 rule, (b) the standard deviation rule and (c) the minimization error rule.

Approach (a) consists in interpreting the wavenumber k_{eff} , for which the filter transfer function has the value $\widehat{G}(k_{eff}; \Delta_{eff}) = 0.5$ as the effective cut-off frequency. The filter width is then related to this frequency simply as $\Delta_{eff} = \pi/k_{eff}$. Therefore, an estimation of the sub-filter resolution parameter Q can be obtained from the previous 1D curves in Fig. 3 by evaluating $Q = \Delta_{eff}/h = \pi/(k_{eff} h) = \pi/\xi_{eff}$. Obviously, considering the constraint $\xi = \eta = \zeta$ is a further source of approximation. Considering the numerical transfer functions induced by the discretizations of the convective terms, we can evaluate that the NSF^{II} , NSV^{II} , SV^{II} schemes produce $Q \cong 1.67$. On the other hand, the schemes NSF^{II-IV} , NSR^{II} , NSR^{IV} results $Q \cong 1.28$, $Q \cong 3.14$ and $Q \cong 1.99$, respectively. Considering the numerical transfer functions induced by discretization of the diffusive terms, we can evaluate $Q \cong 1.14$ for NSF^{II} , NSV^{II} , SV^{II} schemes, $Q \cong 1.02$ for NSF^{II-IV} and $Q \cong 2.83$ for NSR^{II} respectively.

According to method (b) (see Refs. [1–4,6]), by computing the standard deviation of the associated convolution 1D (positive) filter and by expressing the 3D counterpart, the result is

$$(\Delta_{k,eff})^2 = 12 \int_{-\infty}^{+\infty} x_k^2 G_{x_k} dx_k; \quad \Delta_{eff} = \left[\prod_{k=1}^3 (\Delta_{k,eff})^2 \right]^{1/6}, \quad (50)$$

G_{x_k} being the one-dimensional component of the 3D filter kernel along the direction x_k . Hence, by performing an inverse Fourier transform with respect to p' , q' , r' for each of the FV methods previously described the built-in filter kernels $G_{x_k}(x_k - x'_k; \Delta_{k,eff})$ along each x_k direction can be deduced. However, since the inverse Fourier transforms are done on the functions G_j^{FV} , which are composed of an infinite number of non-vanishing Fourier components (the numerical transfer functions are, by definition, truncated by the induced grid cut-off filtering), an approximation is introduced. For the sake of brevity, the analytical expressions of the filter kernels are not reported. The resulting values are reported in Tables 1 and 2 for the convective and diffusive terms respectively. Among the analyzed FV methods, the only one that induces a filter kernel approximating the exact 3D top-hat appears to be NSR^{II} since the built-in filter kernel $G_{NSR^{II}}$ seems a good approximation for $Q \cong 2.29$. Despite the higher accuracy order and the multidimensional implementation, the NSR^{IV} scheme does not appear to induce a suitable approximation of the top-hat filter. Its nature seems more inherent to a higher order discretization of an FD-like derivative, as already partly documented in Ref. [24]. All other schemes suffer from the factorized 1D implementation but it is worthwhile remarking the behavior of the hybrid NSF^{II-IV} scheme since it produces the theoretical expected value $Q = 1$, along each 1D direction.

Table 1

Filter widths evaluation based on method (b) for the six considered FV-based discretization of the convective term.

FV scheme	$\frac{\Delta_{l,eff}}{h}$	$\frac{\Delta_{k,j,eff}}{h}$	$\frac{\Delta_{eff}}{h}$
NSF^{II}	2	0	0
NSV^{II}	$\left\{ \frac{1}{2} \cos[(p_j - l_j)h/2] + 2 \right\}^{1/2}$	0	0
SV^{II}	$\left\{ \frac{\delta_{ij}}{2} \cos[(p_j - l_j)h/2] + 2\delta_{ij} + (1 - \delta_{ij}) \cos(p_i \frac{h}{2}) \cos(l_j \frac{h}{2}) \right\}^{1/2}$	0	0
NSF^{II-IV}	1	0	0
NSR^{II}	2	$\sqrt{2} \cong 2.45$	$\sqrt[3]{12} \cong 2.29$
NSR^{IV}	0	0	0

Table 2

Filter widths evaluation based on method (b) for the considered FV-based discretization of the diffusive term.

FV scheme	$\frac{\Delta_{l,eff}}{h}$	$\frac{\Delta_{k,j,eff}}{h}$	$\frac{\Delta_{eff}}{h}$
NSF^{II}	$\sqrt{2}$	0	0
NSV^{II}	“ “	“ “	“ “
SV^{II}	“ “	“ “	“ “
NSF^{II-IV}	1	0	0
NSR^{II}			

Finally, according to criterion (c), the schemes are analyzed in terms of the errors obtained from Eq. (13). Furthermore, the Fourier coefficients $\widehat{\mathbf{v}}^{\Delta_{\text{eff}}}(p, q, r)$ and $\widehat{\mathbf{v}}^d(p, q, r)$ are assumed to be the same at the given time, so $\mathbf{F}_R - \mathbf{F}_R^d = \mathbf{0}$ is assumed in (12). Thus, the LTE in physical space can be defined as

$$e_{ij}^{\text{FV}}(\mathbf{x}; \Delta_{\text{eff}}) = I \sum_{l,m,n} \sum_{p,q,r} p_j \widehat{E}^{\text{FV}}(p', q', r'; \Delta_{\text{eff}}) \widehat{u}_j^d(p, q, r) \widehat{u}_i^d(l, m, n) e^{I \sum_{k=1}^3 p'_k x_k}, \quad (51)$$

being

$$\widehat{E}^{\text{FV}}(p', q', r'; \Delta_{\text{eff}}) \equiv \widehat{G}_{\mathbf{x}}(p', q', r'; \Delta_{\text{eff}}) - \widehat{G}^{\text{FV}}(p', q', r'; h). \quad (52)$$

In error expression (51), the summation is extended up to the resolvable wavenumbers. Considering each one of the six previously illustrated FV schemes in this error expression

$$\left| \frac{\widehat{E}_j^{\text{NSF}^{\text{II}}}}{\widehat{G}_{\mathbf{x}}} \right| = \left| 1 - \frac{\widehat{G}^{\text{FV}}(p', q', r'; h)}{\widehat{G}_{\mathbf{x}}(p', q', r'; \Delta_{\text{eff}})} \right|, \quad (53)$$

the six errors due to the discretization of the convective terms according to two procedures can be analyzed (again one defines $\xi = p'h$, $\eta = q'h$, $\zeta = r'h$). In the first one, the maximum error is computed while fixing a plane cut to $0 \leq \xi = \eta = \zeta \leq \pi$ (Fig. 4), whereas in the second one (Fig. 5) it is $0 \leq \xi, \eta, \zeta \leq \pi$. Both procedures explore the error values for the range $0.5 \leq Q \leq 2.5$. Consequently, since a single value Q cannot completely eliminate the error for any value (ξ, η, ζ) , the filter width Δ_{eff} is approximately assumed to be the one for which a value Q produces the minimum among the reported maximum errors. Let us observe that a well-recognizable minimum value exists for all schemes except for schemes NSR^{II} and NSR^{IV} . A particular feature, distinguishing curves (a)–(d) from (e)–(f), is in fact that the latter two show practically a constant error (about 100%) until $Q = 2$, the minimum being reached just afterwards. From an inspection of Fig. 5, the same behavior can be deduced for the multidimensional NSR^{II} and NSR^{IV} schemes, while greater errors result from the four other schemes that have no multidimensional reconstruction. Note that the SV scheme, which owing to the staggered velocity collocation requires transversal interpolation, has the lowest errors until $Q = 0.8$.

4. Some real LES computations supplied by an integral-based dynamic modeling: an assessment of the role of the filter parameters

Following the theoretical analysis above, in order for the practical role of the FV-based filter parameters to be assessed, some real LES computations were performed. Firstly, the original extension of the dynamic procedure, developed for the integral form of the equation, is briefly illustrated, (see Refs. [17,42] for more details). After applying the continuous top-hat test-filter of width Δ_{ex} on Eq. (3) we have

$$\frac{\partial \overline{\mathbf{v}}^{\Delta_{\text{eff}} \Delta_{\text{ex}}}}{\partial t} + \overline{\nabla \cdot \mathbf{F}(\overline{\mathbf{v}}^{\Delta_{\text{eff}} \Delta_{\text{ex}}})}^{\Delta_{\text{ex}}} = \overline{\nabla \cdot \mathbf{M}^{\Delta_{\text{eff}} \Delta_{\text{ex}}}}, \quad (54)$$

with

$$\mathbf{M} = \mathbf{F}(\overline{\mathbf{v}}^{\Delta_{\text{eff}} \Delta_{\text{ex}}}) - \mathbf{F}(\mathbf{v}) = (\overline{\mathbf{v}}^{\Delta_{\text{eff}} \Delta_{\text{ex}}} \overline{\mathbf{v}}^{\Delta_{\text{eff}} \Delta_{\text{ex}}} - \mathbf{v}\mathbf{v}) - (2\nu \nabla^S \overline{\mathbf{v}}^{\Delta_{\text{eff}} \Delta_{\text{ex}}} - 2\nu \nabla^S \mathbf{v}), \quad (55)$$

the integral-based exact sub-test scale tensor. Thus, by comparing (55) to the exact unresolved tensor $\mathbf{T} = (\overline{\mathbf{v}}^{\Delta_{\text{eff}} \Delta_{\text{ex}}} \overline{\mathbf{v}}^{\Delta_{\text{eff}} \Delta_{\text{ex}}} - \mathbf{v}\mathbf{v}) - (2\nu \nabla^S \overline{\mathbf{v}}^{\Delta_{\text{eff}} \Delta_{\text{ex}}} - 2\nu \nabla^S \mathbf{v})$, the integral-based resolved tensor, denoted \mathbf{L} in analogy with the classic Leonard tensor, is obtained

$$\mathbf{M} - \mathbf{T} \equiv \mathbf{L} = (\overline{\mathbf{v}}^{\Delta_{\text{eff}} \Delta_{\text{ex}}} \overline{\mathbf{v}}^{\Delta_{\text{eff}} \Delta_{\text{ex}}} - \overline{\mathbf{v}}^{\Delta_{\text{eff}} \Delta_{\text{ex}}} \overline{\mathbf{v}}^{\Delta_{\text{eff}} \Delta_{\text{ex}}}) - (2\nu \nabla^S \overline{\mathbf{v}}^{\Delta_{\text{eff}} \Delta_{\text{ex}}} - 2\nu \nabla^S \overline{\mathbf{v}}^{\Delta_{\text{eff}} \Delta_{\text{ex}}}). \quad (56)$$

Identity (56) represents the counterpart of the Germano identity, here extended to the integral form of the equation [17,42]. It is worthwhile noticing that expression (56) is quite different from the one corresponding to the differential counterpart [1–4]. In particular, let us highlight the presence of the diffusive flux as well as the fact that the quadratic product is not acted upon by the test-filter, the term $\overline{\mathbf{v}}^{\Delta_{\text{eff}} \Delta_{\text{ex}}} \overline{\mathbf{v}}^{\Delta_{\text{eff}} \Delta_{\text{ex}}}$ being indeed absent in (56). This fact is relevant for determining the model coefficient. In fact, the eddy viscosity assumption for modeling the deviatoric part of the tensors (denoted by the subscript *dev*), that is $\mathbf{T}_{\text{dev}} \cong 2\nu_{\text{LES}} \nabla^S \overline{\mathbf{v}}^{\Delta_{\text{eff}} \Delta_{\text{ex}}}$ and $\mathbf{M}_{\text{dev}} \cong 2\nu'_{\text{LES}} \nabla^S \overline{\mathbf{v}}^{\Delta_{\text{eff}} \Delta_{\text{ex}}}$, is introduced. Then, instead of introducing the classical eddy viscosity expression $\nu_{\text{LES}} = C \Delta_{\text{eff}}^2 |\nabla^S \overline{\mathbf{v}}|$, a scaling formulation for the eddy viscosity function, originally developed by Wong and Lilly [48], is now used [41,42]. This model directly adopts the Kolmogorov scaling law that is $\nu_{\text{LES}} = C^{2/3} \Delta_{\text{eff}}^{4/3} \varepsilon^{1/3}$, ε being the dissipation rate, without equating this latter to the energy production. Thus, by assuming the same coefficient and the same rate of dissipation at primary filter and test-level (scale-invariance hypothesis), $\nu_{\text{LES}} = C_e \Delta_{\text{eff}}^{4/3}$ and $\nu'_{\text{LES}} = C_e \Delta_{\text{ex}}^{4/3}$ can be written where $C_e \equiv C^{2/3} \varepsilon^{1/3}$, resulting in a system of five independent equations with a single unknown ν_{LES} that can be determined by using a least square method (see Refs. [1–4,17,42]).

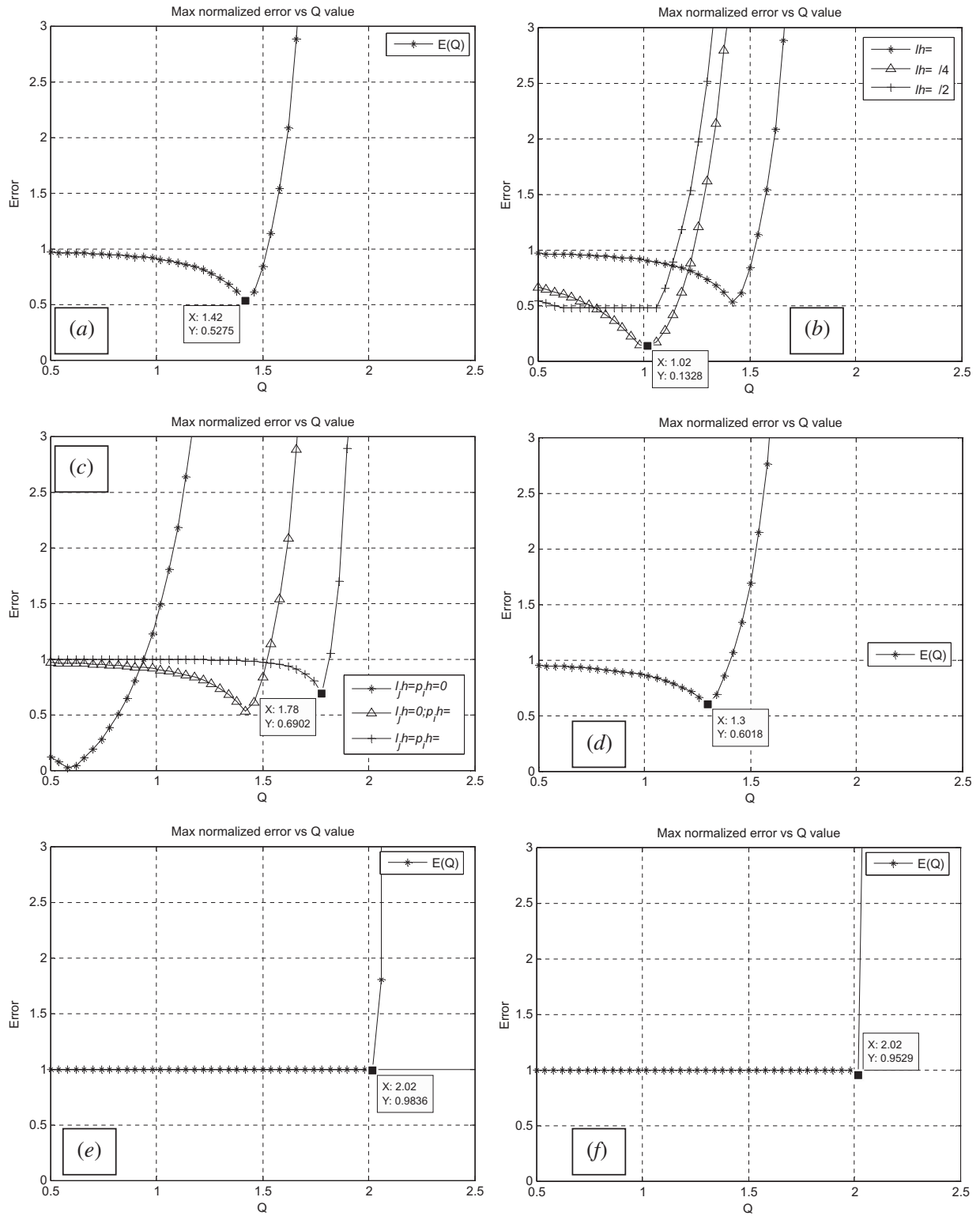


Fig. 4. Normalized maximum error of the discretization of convective terms plotted versus the Q values by defining $\xi = p'h, \eta = q'h, \zeta = r'h$ and forcing the constraint $0 \leq \xi = \eta = \zeta \leq \pi$. (a) NSF^{II} , (b) NSV^{II} , (c) SV^{II} , (d) NSP^{II-IV} , (e) NSR^{II} , (f) NSR^{IV} .

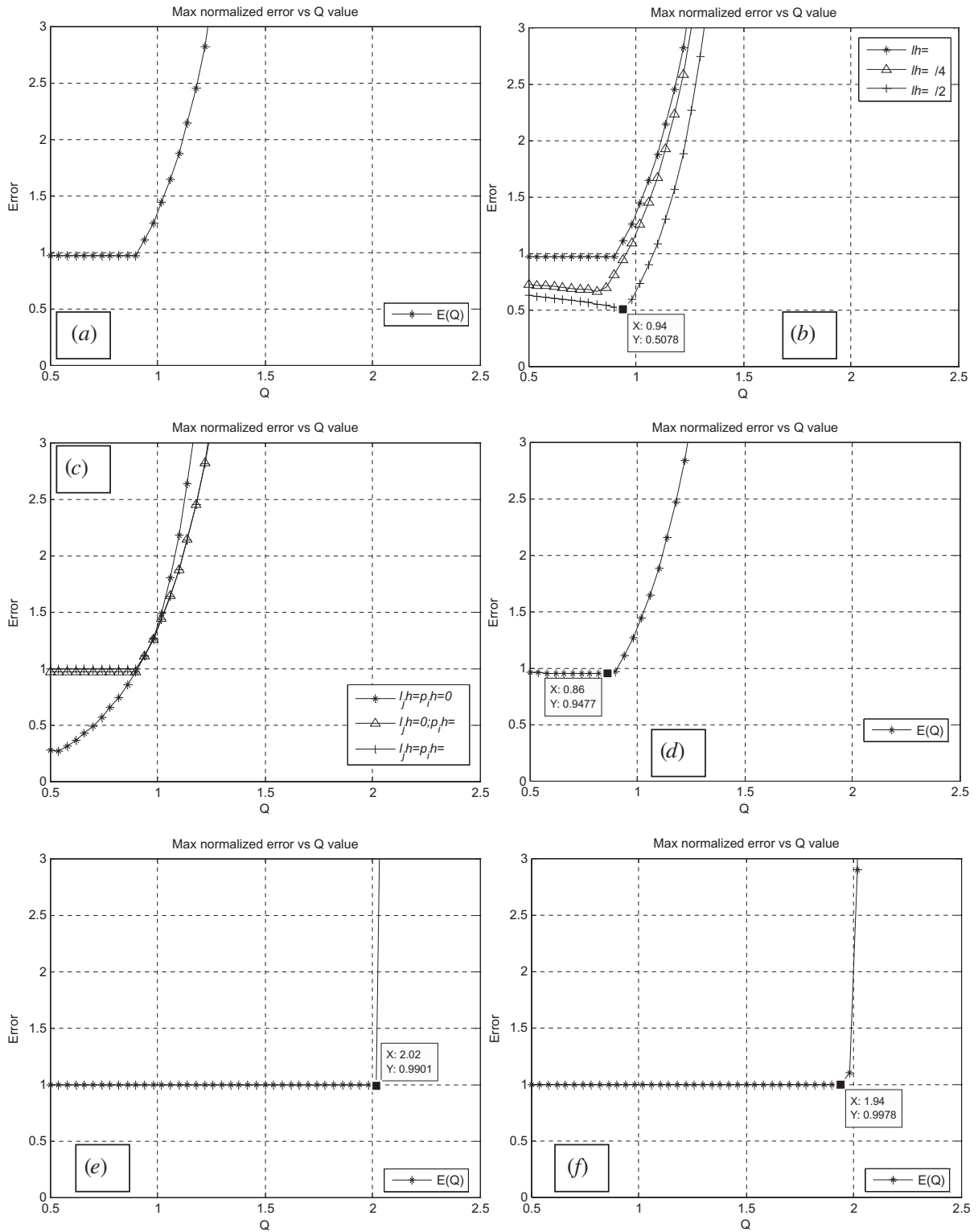


Fig. 5. Normalized maximum error of the discretization of convective terms plotted versus the Q values by defining $\xi = p/h$, $\eta = q/h$, $\zeta = r/h$ for $0 \leq \xi, \eta, \zeta \leq \pi$. (a) NSF^{II} , (b) NSV^{II} , (c) SV^{II} , (d) NSF^{II-IV} , (e) NSR^{II} , (f) NSR^{IV} .

$$v_{LES} = \frac{\mathbf{L}_{dev} : \nabla^s \bar{\mathbf{v}}^{\Delta_{eff}}}{2 \left(\nabla^s \bar{\mathbf{v}}^{\Delta_{eff}} - \alpha^{4/3} \nabla^s \bar{\mathbf{v}}^{\Delta_{eff}} \right) : \nabla^s \bar{\mathbf{v}}^{\Delta_{eff}}} \quad (57)$$

In expression (57), the ratio of the test to FV-based implicit filter width $\alpha = \Delta_{ex}/\Delta_{eff} = \Delta_{ex}/Qh$ is introduced and it is the only input parameter the dynamic procedure depends upon. The relevance of the integral-based identity (56) now appears more evident: the practical determination of $v_{LES}(\mathbf{x}, t)$ does not require that the model viscosity to arbitrarily extracted from the filtering operation, as conversely happens for differential-based LES dynamic formulations [1–4]. Congruently, no additional averaging is required during the computation and (57) can be used to determine a three-dimensional eddy viscosity function.

In actual fact, any LES is a numerical procedure, the computational grid step h and the type of integration scheme being the only user-defined components of the LES solver, the effective filter shape and length being implicitly defined by the chosen type of integration scheme. Thus, the problem is that we do not exactly know the filter length Δ_{eff} . Furthermore, the test-filter length Δ_{ex} , also depends on the type of discretization of the explicit filter. Consequently, the effective filtered velocity is the finite dimensional vector, say $\bar{\mathbf{v}}^d$, which approximates to $\bar{\mathbf{v}}^{\Delta_{eff}}(\mathbf{x}, t)$ and a discrete test-filtered velocity can also be computed, say $\bar{\mathbf{v}}^{d, \Delta_{ex}}$ which approximates to $\bar{\mathbf{v}}^{\Delta_{eff}}(\mathbf{x}, t)$. As recognized in Refs. [1–4,6,16,25,43,44], a suitable input value of the ratio α should be chosen depending on the discrete test filter employed as well as the FV scheme. For instance, Sarghini et al. [44] have demonstrated that better results for the channel turbulent flow can be obtained by properly tuning the value of Δ_{ex}/h according to the effective filter discretization. Therefore, in a real LES computation, the effective eddy viscosity is computed considering the discrete counterpart of the expression (57) and considering $\alpha = \alpha_d(Q, \Delta_{ex}/h)$

$$v_{LES} = \frac{\mathbf{L}_{dev}^d : \nabla^d \bar{\mathbf{v}}^{d, \Delta_{ex}}}{2 \left(\nabla^d \bar{\mathbf{v}}^d - \alpha_d^{4/3} \nabla^d \bar{\mathbf{v}}^{d, \Delta_{ex}} \right) : \nabla^d \bar{\mathbf{v}}^{d, \Delta_{ex}}} \quad (58)$$

4.1. Discretization of the test-filter

Owing to the uncertain value of the filter length $\Delta_{eff} = Qh$, fixing a priori an input value α_d does not tell us, by itself, the way in which the test-filtered velocity $\bar{\mathbf{v}}^{d, \Delta_{ex}}$ must be practically computed on the computational grid. On the other hand, if both a stencil and a discrete formula for computing $\bar{\mathbf{v}}^{d, \Delta_{ex}}$ are fixed a priori, both Δ_{ex}/h and the parameter Q require evaluation to prescribe the proper input value α . In fact, $\alpha_d = \Delta_{ex}/\Delta_{eff} = (\Delta_{ex}/h)/(\Delta_{eff}/h) = (\Delta_{ex}/h)/Q$ therefore, two out of the three computational parameters Δ_{ex}/h , α , Q have to be estimated for a correct setting.

In order to clarify this issue, let us consider as test-filtering a two-dimensional local averaging over a computational grid of uniform steps Δx , Δz according to

$$\bar{\mathbf{v}}^{\Delta_{eff}}(x, y, z, t) = \frac{1}{m^2 \Delta x \Delta z} \int_{z-m\Delta z/2}^{z+m\Delta z/2} dz' \int_{x-m\Delta x/2}^{x+m\Delta x/2} \bar{\mathbf{v}}^{\Delta_{eff}}(x', y, z', t) dx', \quad (59)$$

the test-filtering width Δ_{ex} being a function of Δx , Δz by means of the integer m . Introducing the fourth order accurate 2D extension of the Simpson formula, two discretizations of the (59) are considered for $m = 2$ and 4, over two different local stencils, specifically

$$\left(\bar{\mathbf{v}}_{i,k}^{d, \Delta_{ex}} \right)_{m=2} = \frac{1}{36} \left[16 \bar{\mathbf{v}}_{i,k}^d + 4 \left(\bar{\mathbf{v}}_{i+1,k}^d + \bar{\mathbf{v}}_{i-1,k}^d + \bar{\mathbf{v}}_{i,k-1}^d + \bar{\mathbf{v}}_{i,k+1}^d \right) + \bar{\mathbf{v}}_{i+1,k+1}^d + \bar{\mathbf{v}}_{i-1,k+1}^d + \bar{\mathbf{v}}_{i+1,k-1}^d + \bar{\mathbf{v}}_{i-1,k-1}^d \right], \quad (60)$$

for $m = 2$ over $3\Delta x \times 3\Delta z$ FVs, and

$$\left(\bar{\mathbf{v}}_{i,k}^{d, \Delta_{ex}} \right)_{m=4} = \frac{1}{4} \left[\left(\bar{\mathbf{v}}_{i-1,k+1}^d \right)_{m=2} + \left(\bar{\mathbf{v}}_{i+1,k+1}^d \right)_{m=2} + \left(\bar{\mathbf{v}}_{i-1,k-1}^d \right)_{m=2} + \left(\bar{\mathbf{v}}_{i+1,k-1}^d \right)_{m=2} \right] \quad (61)$$

for $m = 4$ over $5\Delta x \times 5\Delta z$ FVs. Obviously, the effective test-filter lengths induced by (60) and (61) do not exactly coincide with the values theoretically expected from (59) for $m = 2$ and 4. Thus, it is useful to study the behavior of the numerical transfer functions, comparing them to the exact one $\hat{G}^m(\xi, \zeta) = \frac{\sin(m\xi/2) \sin(m\zeta/2)}{(m\xi/2)(m\zeta/2)}$, where $\xi = k_x \Delta x$, $\zeta = k_z \Delta z$. A simple Fourier analysis leads to

$$\hat{G}^{d,m=2}(\xi, \zeta) = \frac{1}{9} (2 + \cos \xi) (2 + \cos \zeta), \quad (62)$$

for formula (60) and

$$\hat{G}^{d,m=4}(\xi, \zeta) = (\cos \xi \cos \zeta) \hat{G}^{d,m=2}(\xi, \zeta) = \frac{\cos \xi \cos \zeta}{9} (2 + \cos \xi) (2 + \cos \zeta), \quad (63)$$

for formula (61), respectively. The graphical representation of the functions is shown in Fig. 6. A numerical evaluation of the errors over the resolved range of frequencies $(\xi, \zeta) \in [-\pi, \pi] \times [-\pi, \pi]$, shows that formula (62) is more accurate than (63), the error being 28% for the former and 36% for the latter. Looking at the distribution of the errors, one can see that formula (63) is

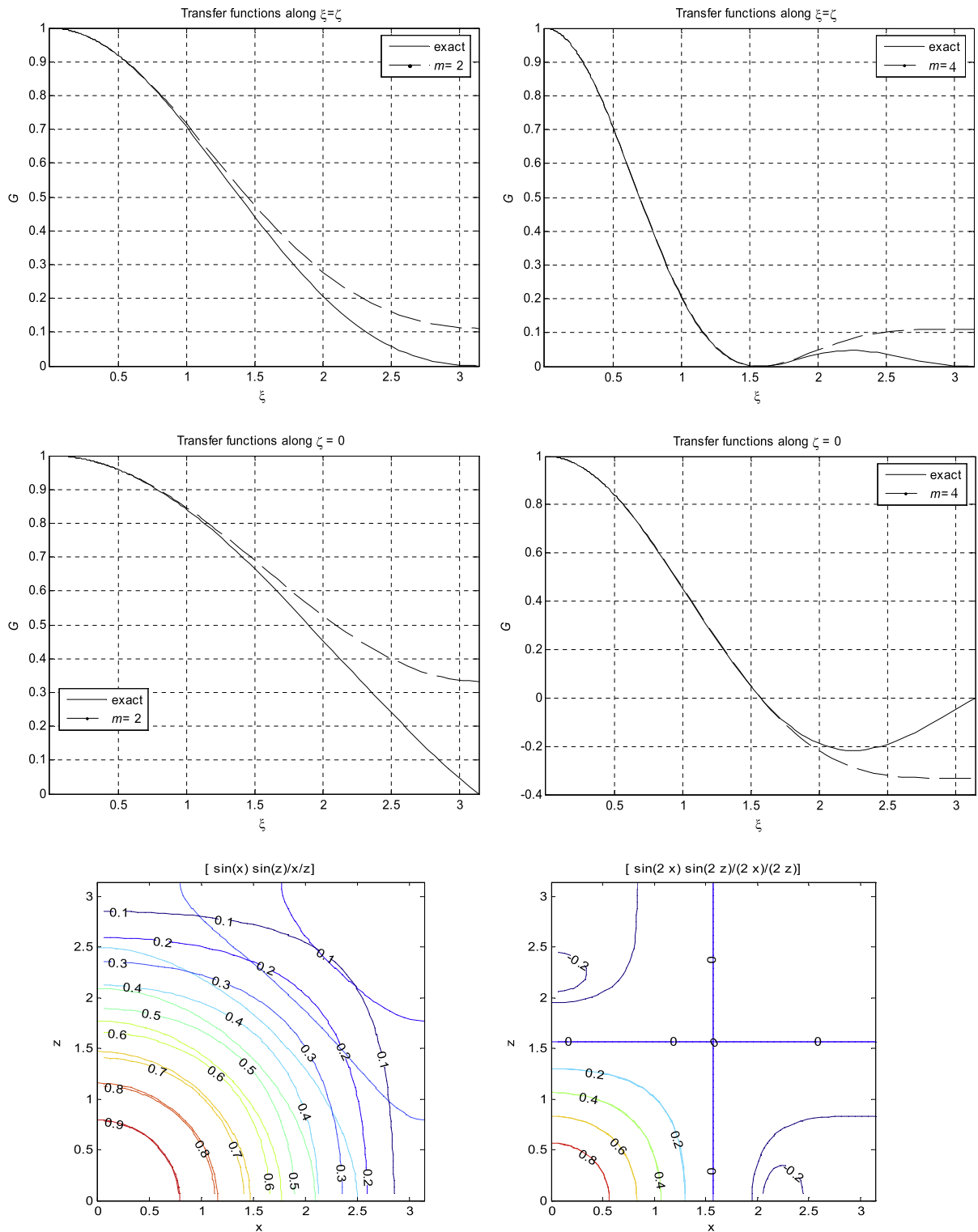


Fig. 6. (a)–(c) Transfer functions of the test-filtering based on the 2D Simpson rule over $3\Delta x \times 3\Delta z$ (left) and $5\Delta x \times 5\Delta z$ (right) plotted versus the analytical one, being $\xi = k_x \Delta x$, $\zeta = k_z \Delta z$. Top figure is for $0 \leq \xi = \zeta = \zeta \leq \pi$.

better than (62) in the lower part of the resolved range, $(\xi, \zeta) \in [0, \pi/2] \times [0, \pi/2]$ but becomes significantly worse in the high-est part $(\xi, \zeta) \in [\pi/2, \pi] \times [\pi/2, \pi]$ of the resolved spectrum.

The induced test-filtering lengths of the two formulas can be estimated according to the approaches analyzed above. Therefore, evaluating the wavenumber k_{eff} for which the transfer function has the value $\hat{G}^{d,m}(k_{\text{eff}}; \Delta_{\text{ex}}) = 0.5$, assuming $h = (\Delta x^2 + \Delta z^2)^{1/2}$ and fixing $\zeta = \zeta$, the result is $\Delta_{\text{ex}}/h = \pi/(k_{\text{eff}} h) = \pi/\zeta_{\text{eff}}$, which leads to $\Delta_{\text{ex}}/h = 2.168$ and 4.51 for (62) and (63), respectively after evaluating ζ_{eff} from the previous curves. Let us note that, using the same criterion, the evaluation of the test-filtering length of the exact expression \hat{G}^m leads to 2.26 and 4.52 for $m = 2$ and 4 , respectively.

In a different approach, according to the procedure reported in Ref. [7] (extended here to two dimensional filtering), an expression of the test-filter width based on the standard deviation of the corresponding discrete filter function is

$$\frac{\Delta_{\text{ex}}}{h} = \sqrt{12 \sum_{I,K} (I^2 + K^2) W_{IK}}, \quad (64)$$

W_{IK} being the coefficients of the discrete filtering expression, centered around the $I, K = (0,0)$ grid point in the homogenous plane x, z . An evaluation of (64) for the coefficients of the Simpson formula over the $3\Delta x \times 3\Delta z$ (case 1) and $5\Delta x \times 5\Delta z$ (case 2) stencils, then produces $\Delta_{\text{ex}}/h = 2\sqrt{2}$ and $4\sqrt{2}$.

The use of implicit filtering in LES has a final consequence on the value α_d that is worth addressing. Several typical turbulent flows possess only some directions of homogeneity and the computational grid is often stretched along the non-homogeneous directions. In such cases, two possibilities can result: either the grid is so fine that resolve all the scales and the non-uniform filtering effect can therefore be disregarded, or the grid is unable to resolve all the scales and filtering effects are present such that Δ_{eff} depends on the position. A typical example of such a case is the LES of turbulent channel flow where the horizontal grid is homogeneous and the normal-wall grid is stretched. If the vertical grid resolves the boundary layer as well as remaining fine enough in the center of the channel, vertical filtering effects could be disregarded and Δ_{eff} is assumed to be constant, depending only on the homogeneous grid sizes. Therefore, if test filtering is only performed along the homogeneous directions, the assumption of a constant value $\alpha_d = \Delta_{\text{ex}}/\Delta_{\text{eff}}$ is justified.

Conversely, the framework becomes more complex if the vertical grid is not fine enough to resolve all scales, for example resolving only the boundary layer with an enlargement of the mesh size in the center of the channel. In such a case, it is common to assume a local dependence of the filter length $\Delta_{\text{eff}} = \Delta_{\text{eff}}(x_i)$, being x_i the non-homogenous direction. If the test filtering is performed along the homogeneous directions, a dependence $\alpha_d(x_i) = \Delta_{\text{ex}}/\Delta_{\text{eff}}(x_i)$ should be properly considered in the dynamic procedure. This hypothesis is not explored in this paper but it is currently the subject of study.

4.2. Simulation of buoyancy-driven turbulence

Some LES results obtained for the buoyancy-driven turbulence test-case are now illustrated. A LES computation with both the second order NSF flux reconstruction¹² and a pseudo-spectral DNS were performed (see Refs. [17,41,42] for details). The primary filtering is considered implicitly applied only to the two-dimensional homogeneous plane $i - k, j$ being the vertical direction that is resolved by a highly refined non-uniform grid such to disregard any vertical filtering effects [17,41,42]. Furthermore, DNS data was post-filtered by applying a horizontal top-hat filtering having length Qh (h is the homogeneous horizontal computational LES grid size) written in differential form [1,17,42],

$$\overline{f_{\text{DNS}}}(\mathbf{x}; Qh) = f_{\text{DNS}}(\mathbf{x}) + \frac{(Qh)^2}{24} \left(\frac{\partial^2}{\partial x'^2} + \frac{\partial^2}{\partial z'^2} \right) \bigg|_{(x',z')=(x,z)} f_{\text{DNS}}(\mathbf{x}') + \dots \quad (65)$$

extended up fourth order terms. The DNS-based eddy viscosity function was then evaluated according to

$$\nu_{\text{FDNS}}(\mathbf{x}; Qh) = \frac{[2(\nabla^s \nabla_{\text{DNS}} - \nabla_{\text{DNS}} \nabla_{\text{DNS}}) + (\nabla_{\text{DNS}} \nabla_{\text{DNS}} - \nabla_{\text{DNS}} \nabla_{\text{DNS}})] : \nabla^s \nabla_{\text{DNS}}}{2(\nabla^s \nabla_{\text{DNS}} : \nabla^s \nabla_{\text{DNS}})}. \quad (66)$$

First, let us hypothesize disregarding the effect of the sub-filter parameter Q , where only $\Delta_{\text{eff}} = h$ is considered. The classical values $\alpha_{d,1} = 2$ and $\alpha_{d,2} = 4$ are then prescribed in (58) for cases 1 and 2, respectively. The two resulting horizontally averaged vertical profiles of the eddy viscosity function $\langle \nu_{\text{LES}} \rangle$ are plotted in Fig. 7(a) and compared to the counterpart profiles $\langle \nu_{\text{FDNS}} \rangle$, obtained by computing (66) for the values $Q = 1$ and 1.8 . It is evident that both LES profiles largely overestimated that of the DNS at $Q = 1$ whilst almost agree with the profile obtained for $Q = 1.8$.

Hence, a more careful analysis requires an evaluation of the effect of Q on the LES computations. With regard to (64), for example, the values $\Delta_{\text{ex},1}/h = \alpha_{d,1}Q = 2\sqrt{2}$ and $\Delta_{\text{ex},2}/h = \alpha_{d,2}Q = 4\sqrt{2}$ were estimated for cases 1 and 2, respectively. In the previous LES computations it is implicitly assumed that a value $Q = \sqrt{2}$ is induced by the discretization. However, it results because of the somewhat arbitrary choice of α_d .

Hence, to infer the role of the value Q more effectively in the dynamic LES computation, instead of prescribing a value α_d a priori, another group of runs were performed while fixing the value $Q = 1.8$. Specifically $\alpha'_{d,1} = \frac{1}{Q} \frac{\Delta_{\text{ex},1}}{h} = \frac{2\sqrt{2}}{1.8} = 1.57$ and $\alpha'_{d,2} = \frac{1}{Q} \frac{\Delta_{\text{ex},2}}{h} = \frac{4\sqrt{2}}{1.8} = 3.14$ are then set. Furthermore, a computation for $Q = 1$, which assumes that $\alpha''_{d,2} = \frac{1}{Q} \frac{\Delta_{\text{ex},2}}{h} = \frac{4\sqrt{2}}{1} = 5.66$, was also considered. The resulting profiles of the eddy viscosity are compared in Fig. 7(b) along with those of the filtered

¹² It is worthwhile observing that, owing to the need to compute a divergence-free velocity field, the adopted flux reconstruction is slightly different in order to avoid spurious oscillations (see Ref. [26]).

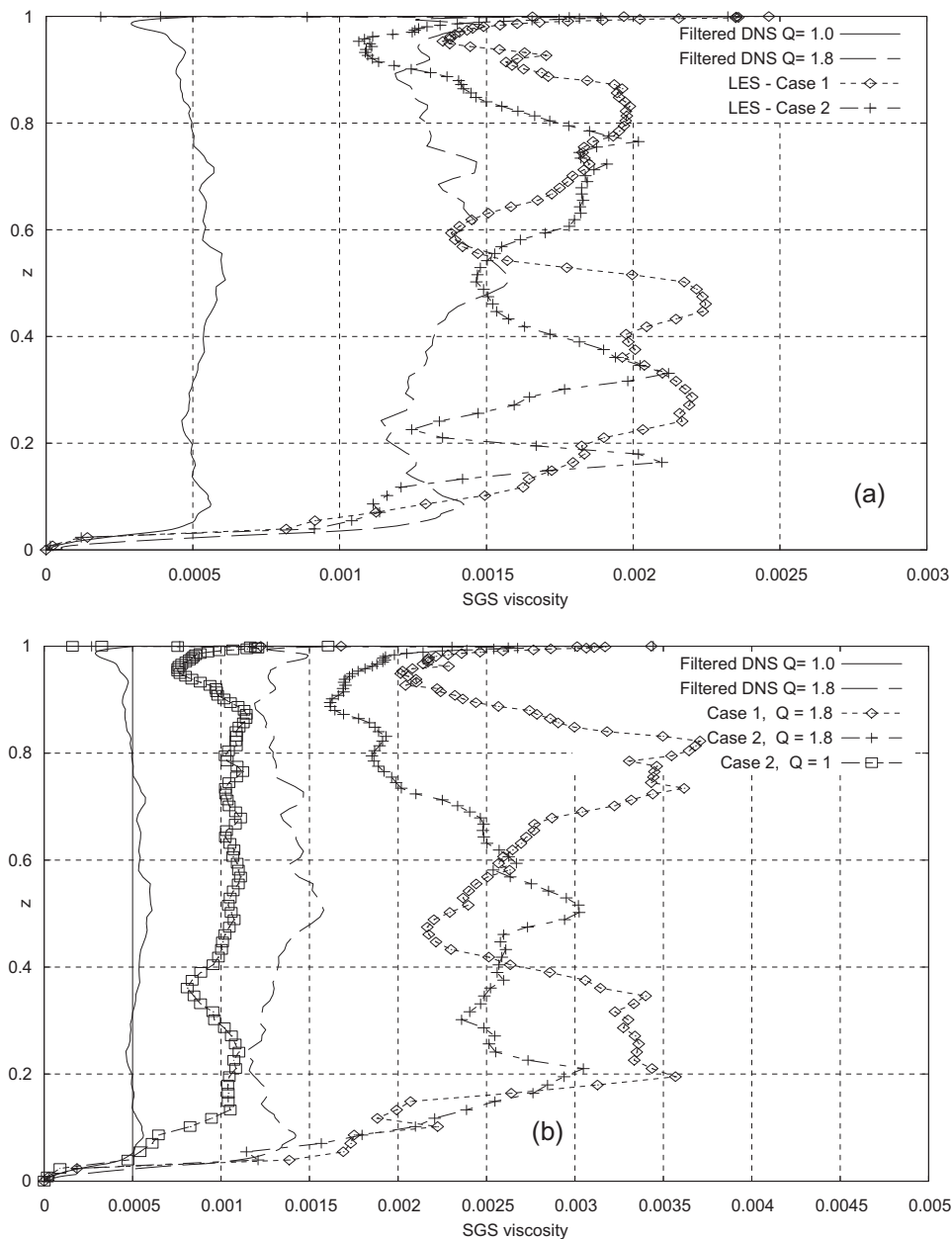


Fig. 7. LES computations of buoyancy-driven turbulence. Horizontally averaged vertical profiles of the SGS viscosity $\langle \nu_{LES} \rangle$ for second order accurate FV-based LES compared to the post-filtered ($Q = 1.0$ and 1.8) DNS counterpart (ν_{DNS}). (a) The values $\alpha_{d1} = 2$ and $\alpha_{d2} = 4$ are arbitrarily prescribed. (b) The values $\alpha'_{d1} = 1.57$, $\alpha'_{d2} = 3.14$ ($Q = 1.8$) and $\alpha'_{d2} = 5.66$ ($Q = 1$) are used.

DNS. It is important to observe the consequent increasing of the profiles at $Q = 1.8$, indicating an excess of SGS viscosity. Hence, it can be deduced that, as observed from the previous 3D theoretical analyses, the value $Q = 1.8$ is over-estimated for the NSF discretization. On the other hand, the profile obtained with α'_{d2} lies in between the two filtered DNS solutions. In addition, the same comparison of the eddy viscosity profiles between LES computations and post-filtered DNS data was reported in Ref. [42] (where a spectral cut-off with $\Delta_{ex} = 4h$ was used), perhaps highlighting a much greater discrepancy. However, it is well known that post-filtered DNS data does not always correlate well to LES data for long-term integration.

4.3. Simulation of turbulent channel flow at $Re_\tau = 590$

A further assessment of the role of the filter parameters on the LES solution is obtained by examining the classical problem of the plane channel turbulent flow at $Re_\tau = 590$ for which several existing LES and DNS databases can be used (see Ref.

[46]). The example of SM-based (which induces the application of a projective filter) LES solution was already presented in Fig. 1, showing that it produced an overshoot in the velocity profile. The dynamic SGS model used in the spectral code is based on the scaling law model rather than the classic Smagorinsky. Furthermore, the spectral code has a hyperviscosity-based explicit filtering procedure (see Ref. [41]), that is activated each N time-step and independent from setting DNS or LES. We tested the resulting additional dissipation effects that can be restricted to a certain extent using an N value of about 30, since setting a greater value produced numerical oscillations close to the Nyquist frequency. Some more details about the spectral LES can be found also in Ref. [42]. In Fig. 1 the FV-based solution shows a lower velocity profile. Therefore, an investigation of the role of the type of filtering and type of modeling can give some insight.

The dependence of the solutions (the same FV-based second order method is used) upon two parameters are now analyzed: (a) the computational length h (that is, the induced filter length $\Delta_{\text{eff}} = Qh$); (b) the chosen value of the parameter α_d . To this end, three computational grids were used, all of them having 64 grid points non-uniformly distributed in the vertical direction such that the first computational node near the walls is located at $y^+ \approx 0.33$. The boundary layer is resolved but the trigonometric stretching law enlarges the grid size along the wall-normal direction in the center of the channel, causing some filtering effects in the non-uniform direction. In stream-wise and span-wise directions the grids are uniform, built of 32×42 (Coarse grid – CG), 48×64 (Mid grid – MG) and 64×80 (Fine grid – FG) FVs, respectively. The computational mesh sizes in wall-units are $\Delta x^+ \approx 116$, $\Delta z^+ \approx 44$, $\Delta x^+ \approx 77$, $\Delta z^+ \approx 29$ and $\Delta x^+ \approx 58$, $\Delta z^+ \approx 23$, for CG, MG and FG respectively. The computational time step is fixed for all cases to $\Delta t = 5 \times 10^{-5}$, the run being performed until an energy equilibrium is achieved after which the samples of the fields are memorized for computing the statistical time averaging. A constant pressure gradient is used as a forcing term. For the sake of completeness, a no-model simulation is also performed on each one of the three grids.

The discrete test-filtered velocity is computed according to (60) (case 1) and (61) (case 2) respectively, and for each grid, the solutions were obtained for a set of three chosen values: $\alpha_d = 2, 3, 4$ and $\alpha_d = 3, 4, 5$, assumed for cases 1 and 2, respectively. The resulting statistically averaged stream-wise velocity profiles (for the sake of brevity higher order statistics are not reported) are organized in Fig. 8, from top to bottom for CG, MG and FG, respectively. The no-model and DNS solutions are superimposed. Case 1 is shown on the right and case 2 on the left.

Firstly, in the framework of implicit filtering, it is worthwhile remarking that while diminishing h the effective filter width $\Delta_{\text{eff}} = Qh$ is accordingly reduced. Thus, in a grid-refinement study, there is no convergence towards a filtered solution, as it is discussed in Ref. [51]. In other words, for each k th computational step size h_k , there is a different characteristic filter length parameter and, consequently, a different class of filtered velocity field $\bar{\mathbf{v}}^d(Qh_k)$ to be compared to $\bar{\mathbf{v}}(\mathbf{x}, t; \Delta_k)$. It is therefore not possible to distinguish clearly between the effects due to the reduction of the local truncation error magnitude and those due to the reduction of the filtering length. The only proper behavior to be expected is that, for vanishing computational size, the LES solution must tend towards the DNS, as seen in Fig. 8. In order to discern only the effect of the numerical errors at different grid resolutions the “explicit filtering” approach should be used, taking a fixed filter length and diminishing only the computational step size [51]. This approach naturally means that the convergence is towards an “ideal” solution of a continuous filtered equation and no longer towards the DNS. According to Pope’s questions stated in Ref. [45], these aspects distinguish the “pure physical LES”, the “physical LES” and the “numerical LES”.

The plotted results show that the slopes of the curves are strongly affected both by the choice of the grid size and the extension of test filtering and parameter α_d . Of course, the results presented on CG and AG did not mean that a physically reliable LES solution is already obtainable at low resolution, the averaged velocity profiles appearing far from the DNS one. However, is interesting to observe the trend for combined grid and filtering values. A general trend, which can be observed in all results, is that the solution improves as the value of α_d is increased and the test filtering stencil is reduced. For case 2, a systematic deviation from the logarithmic slope can be seen as well as a considerable overshoot of the DNS curve. An improvement is obtained only for the FG and high values α_d . This effect is partially justified by the fact that the greater test-filter width on CG and MG results in a wavenumber cut-off that lies in a critical part of the inertial range where the scale-invariance hypothesis is less justified. For case 1, a minor overshoot is found and the profiles agree better with the logarithmic slope. Value $\alpha_d = 2$, perhaps a commonly adopted value in LES (for example it is the default value prescribed in some commercial FV-based codes), produces the worst solution, whilst $\alpha_d = 4$ provides the best.

It is worthwhile observing the behavior of the FV-based no-model simulation. It is energy-stable on a coarse grid and for second order central (co-located) schemes for which methods are generally considered unstable. In principle, a no-model simulation should produce wrong dynamics since the unresolved terms are simply disregarded and only the smoothing implicitly induced by the FV method is present. In fact, the velocity profiles have some overshoot in the logarithmic region with a deviation in the slope for CG and MG (as well as a non-monotone decaying of the energy spectra). Conversely, the no-model solution computed on FG shows a velocity profile that is quite in agreement with the DNS solution. Thus, one wonders what the eddy viscosity model would really do to further improve the no-model result on this grid. The effect of the turbulence model appears in a consequent increasing of the stream-wise velocity profiles, overestimating that of the DNS. Therefore, adding the eddy viscosity contribution, the overshoot in the logarithmic region should not merely be considered an error but it is somehow congruent to the implicit top-hat filtered velocity. In actual fact, there are also no theoretical reason to expect an exact concordance between the statistically averaged LES velocity and the logarithmic law produced by DNS, see Ref. [47]: “the analytical form of the law of the wall is not necessarily invariant to a filter operation since the friction velocity of filtered data can be different from the unfiltered data”.

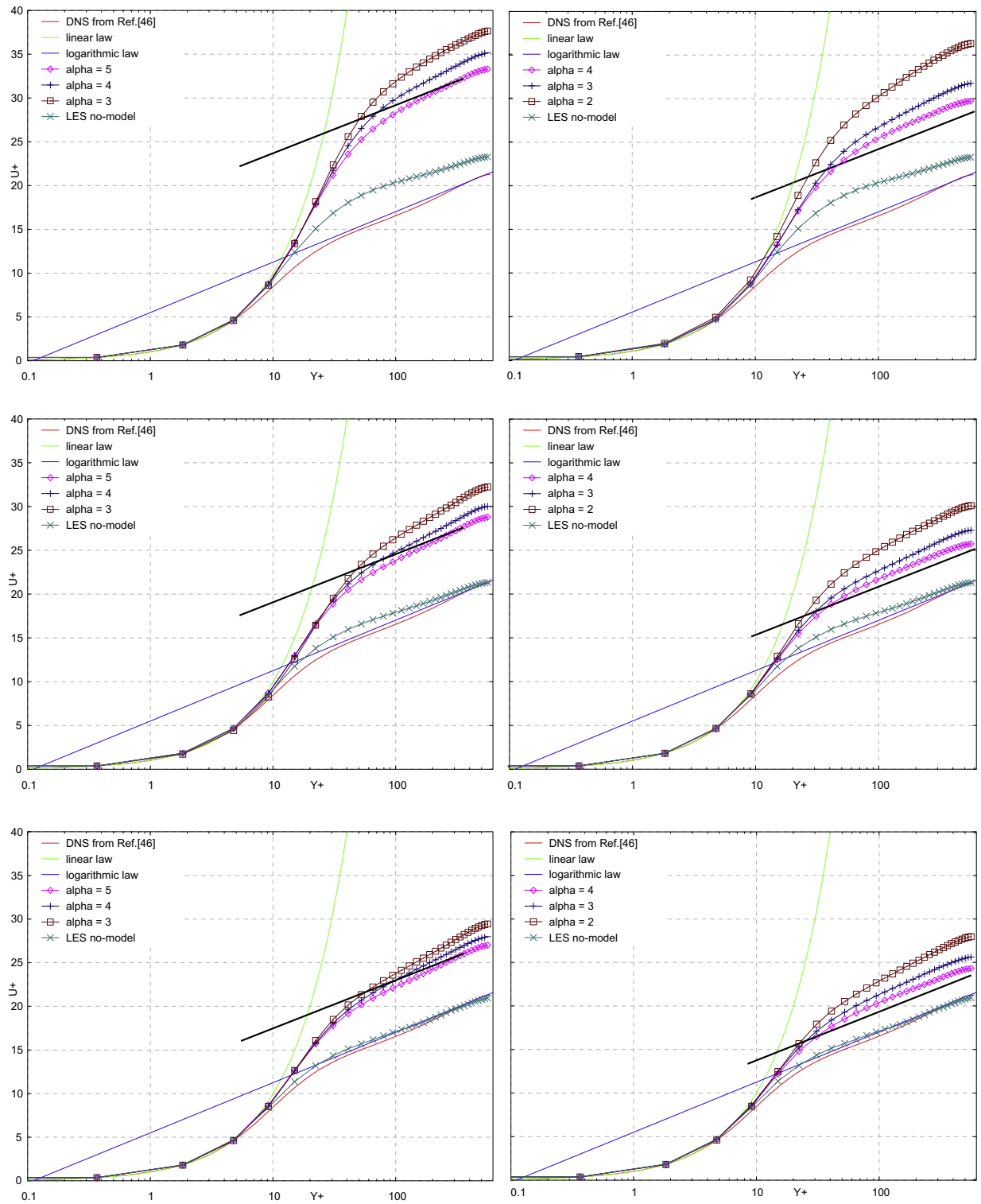


Fig. 8. LES computations of turbulent channel flow at $Re_\tau = 590$. Statistically averaged stream-wise velocity profiles for (from top to bottom) Coarse Grid, Mid Grid, Fine Grid. Right column case 1, left column case 2. DNS data are taken from Ref. [46].

Moreover, several tests on channel flow at a high Reynolds number, exploiting several LES models, are reported by Sarghini et al. in Ref. [44]. Specifically, static and dynamic versions of the Smagorinsky eddy viscosity model were tested while using a spectral method on a $64 \times 97 \times 128$ grid. A no-model simulation was also produced. Comparison to (unfiltered) DNS

data shows high variation, in the range $\pm 20\%$. All models give a somewhat high intercept of the logarithmic layer. Acceptable results are only obtained while using scale-similar models. In addition, the sensitivity of the mean velocity to the test-filtering parameters is clearly observed. However, the correct amount of overshoot in the velocity profile due to the action of the SGS model is somehow undetermined.

Finally, Meyers et al. [50] discussed the optimal locus of the computational parameter where overestimation can be reduced.

A further key-issue concerns the span-wise resolution used. The significance of increasing the resolution along the span-wise direction has to be taken into account¹³. Some results demonstrated that the overshoot of the velocity profile is reduced by increasing the number of cells in the span-wise direction, much more than can be achieved by increasing the normal-to-wall resolution. It is generally accepted that such sensitivity is due to the improved resolution of the streaks. This fact is in agreement to the interpretation that a different filtered solution is achieved while increasing the span-wise grid size.

The amount of overestimation and the different slope of the velocity profiles in Fig. 8 could be attributed also to the particular choice of the eddy viscosity scaling law $\nu_{LES} = C^{2/3} \Delta_{eff}^{4/3} \epsilon^{1/3}$, as such scaling is not necessarily well-suited in the non-homogeneous part of the flow. Thus, in order to assess to what extent the results depend upon the filter parameters or on the model law, a further set of LES run, this time with the classic¹⁴ eddy viscosity model $\nu_{LES} = C \Delta_{eff}^2 |\nabla^s \bar{\mathbf{v}}^{\Delta_{eff}}|$, was performed. This model is deduced prescribing an equilibrium between energy production and dissipation, well-suited in channel flows. It is worthwhile remarking that, the eddy viscosity function is again deduced from the new integral-based identity (56),

$$\nu_{LES} = \frac{\mathbf{L}_{dev}^d : \nabla^d \bar{\mathbf{v}}^{\Delta_{ex}}}{2 \left(\nabla^d \bar{\mathbf{v}}^d - \alpha_d^2 \frac{|\nabla^s \bar{\mathbf{v}}^{\Delta_{ex}}|}{|\nabla^s \bar{\mathbf{v}}^d|} \nabla^d \bar{\mathbf{v}}^{\Delta_{ex}} \right) : \nabla^d \bar{\mathbf{v}}^{\Delta_{ex}}} \quad (67)$$

and all the described advantages on its full three-dimensional character and absence of mathematical inconsistency are thus maintained. In order to investigate the effect due to the two modeling laws, which can be seen as the SGS error term in (12), three simulations were performed on the Coarse Grid for the case 1, selecting $\alpha_d = 2, 3, 4$. The statistically averaged stream-wise velocity profiles are reported in Fig. 9. For the sake of clarity, the plots of the DNS and no-model simulation were superimposed. Again, the best agreement with DNS is obtained while using $\alpha_d = 4$, which is twice the classical adopted choice $\alpha_d = 2$. It is therefore confirmed that the dependence of statistics is only partially related to the type of SGS modeling, a dependence should be attributed to the shape of the filter implicitly induced by the FV scheme as well as to the explicitly computed test-filtered velocity.

Finally, a brief investigation of the effects of the variable filter width, implicitly induced by the non-uniform vertical grid, was performed. The vertical grid was reduced to 32 non-uniform cells but the horizontal resolution is fine, using 64×64 cells in the homogeneous plane. This way, the first grid point close to the wall was outside the viscous sub-layer being at $y^+ = 1.42$, while the other step sizes were $\Delta x^+ = 58$, $\Delta z^+ = 29$. Three LES runs were performed: the no-model case, the case with the eddy-viscosity model (58) and the (67). The parameter $\alpha_d = 3$ was fixed. Even if the boundary layer was not solved by the grid, the no-slip boundary condition at walls was prescribed. The results are shown in Figs. 9 and 10, which reports the statistically averaged stream-wise velocity profiles, eddy viscosity profiles and stream-wise energy spectra. Again, despite the unresolved boundary layer, the no-model velocity profile shows a quite surprising agreement with DNS, the overestimation always being obtained when the eddy viscosity models is supplied. On the other hand, the stream-wise energy spectra are clearly better when using the SGS model, recovering the low wavenumber energy content (such effect is present also in all previous simulation). Despite the very coarse grid, the absence of any energy pile-up in the no-model simulation demonstrates the effective presence of the smooth filter implicitly induced by the FV scheme.

The importance of recognizing the dependence of LES calculations on the numerically induced filter width or, more generally, the turbulence resolution length scale was addressed by Pope [45]. The statistics of implicit filtering-based LES solutions were demonstrated to be affected by numerical resolution for ratios of filter-to-grid length lower than 4, as holds for the present subgrid resolution ratio Q . It can be concluded that reducing the grid size, which is the linked filter length, alters the statistics, unless the energy-containing eddies are completely resolved by the numerical grid.

5. Further tasks and conclusions

An exhaustive assessment of a theory for implicit filtering in integral-based LES requires elements that could not be discussed in this paper but that will be the subject of future studies.

The first element is clearly the comprehensive treatment of the Navier–Stokes system of equations while solving incompressible turbulent flows. It must therefore be taken into account that the presence of the pressure gradient and the effect of the projection methods in terms of the (time–space) filtering cannot be disregardable [26,29,31–33]. Moreover, the practical use of FV-based LES is often devoted to the simulation of turbulent flow problems that are not homogeneous in some or all of

¹³ A reviewer confirmed that better results are achieved by using a spectral LES code with a $48 \times 65 \times 96$ grid supplied by a standard dynamic Smagorinsky model.

¹⁴ A reviewer suggested to check for the overshoot of the profiles by introducing the classic Smagorinsky model in the new integral-based Germano identity.

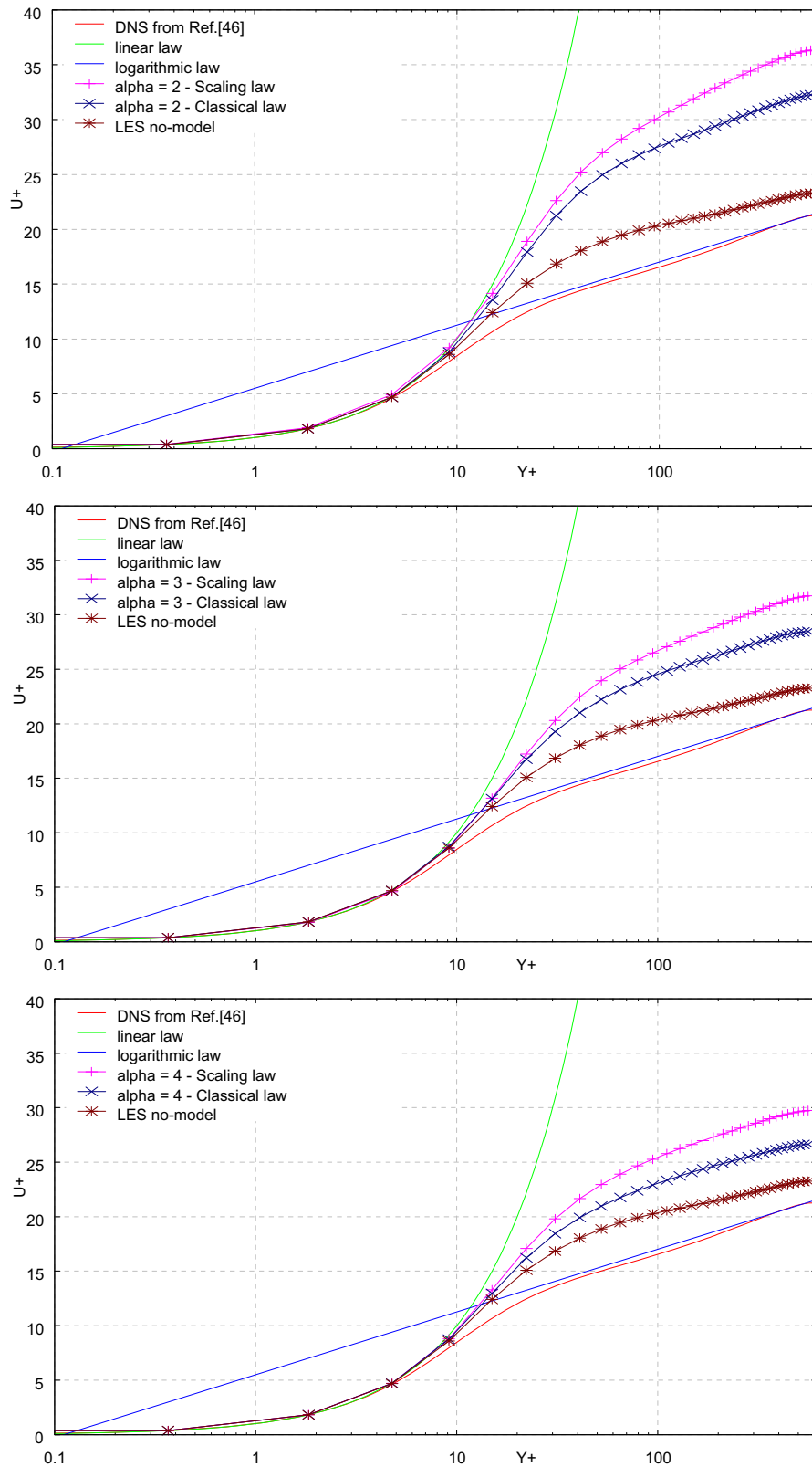


Fig. 9. LES computations of turbulent channel flow at $Re_\tau = 590$ on the Coarse Grid for the case 1. Comparison between the statistically averaged streamwise velocity profiles obtained by means of the classical Smagorinsky eddy viscosity $\nu_{LES} = C\Delta_{eff}^2 |\nabla^s \mathbf{v}|$ and the scaling-based one $\nu_{LES} = C^{2/3} \Delta_{eff}^{4/3} \epsilon^{1/3}$.

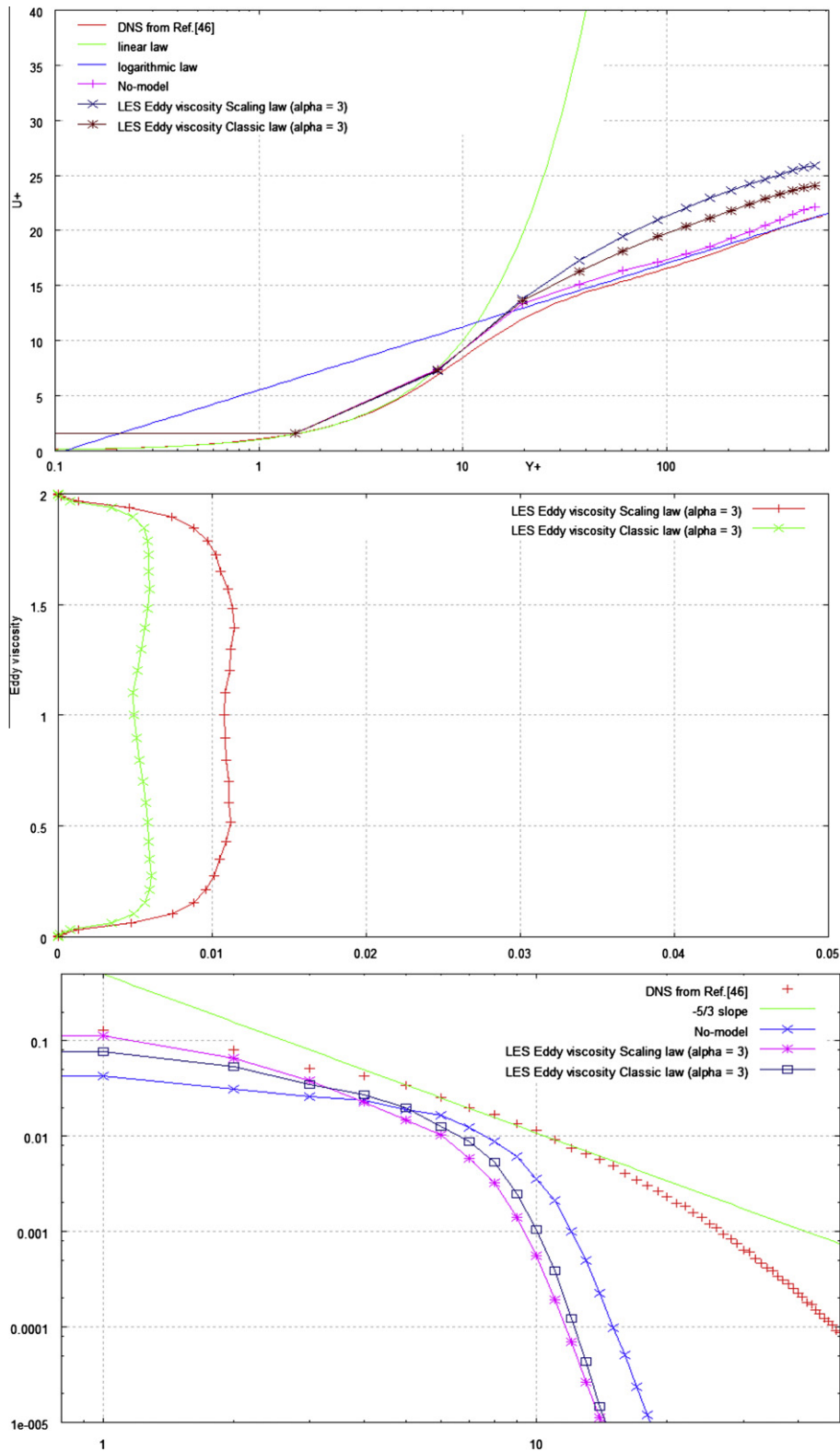


Fig. 10. LES computations of turbulent channel flow at $Re_\tau = 590$. Effects of the coarseness vertical grid with non-resolved boundary layer for three LES cases: no-model, classical Smagorinsky eddy viscosity $\nu_{LES} = C\Delta_{eff}^2 |\nabla^2 \mathbf{v}|$ and the scaling-based one $\nu_{LES} = C^{2/3} \Delta_{eff}^{4/3} \epsilon^{1/3}$. The parameter $\alpha_d = 3$ was fixed. From top to bottom, statistically averaged stream-wise velocity profiles, eddy viscosity profiles, stream-wise energy spectra at $y^+ = 590$.

the spatial directions along which a non-uniform computational grid (or non-structured grid) is used. A scheme applied on variable computational step-size induces implicitly filtering associated with a non-homogeneous width and the previous analysis must be extended to anisotropic FV-based discretizations. Let us once again highlight the advantage that there is no requirement to commute filtering and derivative, provided that the correct integral governing equation and flux decomposition are considered.

The computational FV of measure $h \times h \times h$ is generally the most adopted volume to compute the averaged variable but this leads to a low Q value. Actually, the proper use of the integral-based FV methods for LES would allow for a possible increasing of the Q value, while introducing the explicit filtering [51] in a more natural way. In fact, while taking the cell size separated from the filter length, additional neighboring computational cells can be used to construct a FV having a greater measure. For example, a $3h \times 3h \times 3h$ FV, requiring the use of the discrete operators $I_{x-3h/2}^{x+3h/2}$, $I_{y-3h/2}^{y+3h/2}$ and $I_{z-3h/2}^{z+3h/2}$, can be used. The fluxes over the greater surfaces $3h \times 3h$ can be built simply by exploiting the additive property of the fluxes computed over the smallest surface $h \times h$. Of course, independently from the FV extension, the number of total computational equations must remain the same, therefore overlapping FVs must be used. However, owing to the uniqueness of the numerical flux function, the discrete conservation property is saved. Such a technique can result in a greater efficiency than the explicit filtering procedure, perhaps being that a peculiarity unique of the integral-based FV formulation, FD or SM cannot sharing such an advantage. This procedure needs to be explored and will be illustrated in future studies.

A further task involves addressing the effective role of the built-in transfer functions in controlling aliased frequencies that appear from the non-linear velocity product [20–23]. Note that the exact transfer function in (17) is expressed in terms of the wavenumbers p' , q' , r' , the sums extending to an infinite number of Fourier components. A comparison is then made of the numerical transfer functions induced by the discretizations, which are limited to a finite numbers of components. Therefore, the task of understanding the filtering effects on the Fourier coefficients, depending separately on p , q , r and l , m , n , already exists in analyzing the continuous exact form. Clearly, if the exact (continuous) transfer function by alone cannot control all the aliased frequencies, an FV method cannot be more efficient than the continuous counterpart, even if it is discretized congruently. Any kind of implicit filtering would somehow be limited in its efficiency.

As conclusion, some lessons from this study can be addressed. Any FV method, when congruently implemented as a discrete form of the integral governing equation must induce a built-in filtering that is an exclusive approximation of the top-hat filter. Analysis of other filter types used as a reference (e.g. the spectral cut-off) produce a discrepancy that is not an error due to discretization. It is worthwhile remarking that the supportive comparisons between LES and DNS data are more realistic when DNS fields are post-filtered by means of a filter function that mimics at best the implicit filter in effect during the LES. This implied that the SGS terms computed from filtered DNS are more indicative of the effective scale separation. On the other hand, the analysis generated ample information provided that a fully three-dimensional framework is used. The simple one-dimensional approximation may seem somewhat misleading. In order for a FV-based method to produce an accurate built-in representation of the continuous top-hat filter, the accuracy of the flux reconstruction must be improved and not of the discrete derivative as is frequently done for FD-based methods. Indeed, it was shown that hybrid discretizations cause a difficult and not univocal interpretation of the built-in filter in effect. The consequences of hybridization appear in the different approximations towards either the identity operator or that of the top-hat affecting the practical scales separation and the consequent SGS modeling. It was shown that the optimal choice of the test-filter width for an SGS procedure is influenced by the effective width of the built-in primary filter. Recognizing a priori a suitable value of the sub-filter resolution parameter Q enables us to properly construct the explicit test-filter width. Conversely, understanding that a higher order FD discretization scheme induce a higher order filter, the transfer function of which tends to the unity operator, should be properly considered in terms of a deconvolution-based top hat filtering that tries to mimic the effect of the sharp cut-off filtering.

Acknowledgments

The author would like to acknowledge the CINECA consortium (Casalecchio sul Reno – Bologna, Italy) which provided computational time on IBM SP6.

This study is partly developed within the framework of the *LESinItaly* project involving a number of Italian academic groups (web site currently being built http://mwiki.caspar.it/mwiki/index.php/Main_Page?w=cfd).

References

- [1] P. Sagaut, Large Eddy Simulation for Incompressible Flows. An Introduction, third ed., Springer, 2006.
- [2] L. Berselli, T. Iliescu, W. Layton, Mathematics of Large Eddy Simulation of Turbulent Flows, Springer, 2005.
- [3] M. Lesieur, O. Métais, P. Comte, Large-Eddy Simulations of Turbulence, Cambridge, 2005.
- [4] B.J. Geurts, Elements of Direct and Large-Eddy Simulations, Edwards, 2004.
- [5] T.S. Lund, H.-J. Kaltembach, Experiments with explicit filters for LES using a finite-difference method, Center for Turbulence Research, Ann. Research Briefs, Stanford University, 1995, pp. 91–105.
- [6] T.S. Lund, On the use of discrete filters for large eddy simulation, Center for Turbulence Research, Ann. Research Briefs, Stanford University, 1997, pp. 83–95.
- [7] A.W. Vreman, B.J. Geurts, A new treatment of commutation-errors in large-eddy simulation, Adv. Turb., Proc. IX European Turbulence Conferences, 2002.

- [8] J. Gullbrand, F.K. Chow, The effect of numerical errors and turbulence models in large-eddy simulations of channel flow, with and without explicit filtering, *J. Fluid Mech.* 495 (2003) 323–341.
- [9] T. Brandt, A priori tests on numerical errors in large eddy simulation using finite differences and explicit filtering, *Int. J. Numer. Methods Fluids* 51 (2006) 635–657.
- [10] K. Mahesh, G. Constantinescu, P. Moin, A numerical method for large-eddy simulation in complex geometries, *J. Comput. Phys.* 197 (2004) 215–240.
- [11] R.J. LeVeque, *Finite Volume Methods for Hyperbolic Problems*, Cambridge Press, 2002.
- [12] J.H. Ferziger, M. Peric, *Computational Methods for Fluid Dynamics*, Springer, 2001.
- [13] G. De Stefano, F.M. Denaro, G. Riccardi, High order filtering for control volume flow simulations, *Int. J. Numer. Methods Fluids* 37 (2001) 7.
- [14] P. Iannelli, F.M. Denaro, G. De Stefano, A deconvolution-based fourth order finite volume method for incompressible flows on non-uniform grids, *Int. J. Numer. Methods Fluids* 43 (4) (2003) 431–462.
- [15] A. Arovitola, F.M. Denaro, On the control of the mass errors in finite volume-based approximate projection methods for large eddy simulations, in: J. Meyers, B. Geurts, P. Sagaut (Eds.), *Quality and Reliability of Large-Eddy Simulations*, ERCOFTAC Series, vol. 12, Springer, 2008.
- [16] J. Meyers, B.J. Geurts, P. Sagaut, A computational error-assessment of central finite-volume discretizations in large-eddy simulation using a Smagorinsky model, *J. Comput. Phys.* 227 (2007).
- [17] F.M. Denaro, G. De Stefano, D. Iudicone, V. Botte, A finite volume dynamic large-eddy simulation method for buoyancy driven turbulent geophysical flows, *Ocean Model.* 17 (3) (2007) 199–218.
- [18] S. Hickel, N.A. Adams, Analysis of truncation errors and design of physically optimized discretizations, in: J. Meyers, B. Geurts, P. Sagaut (Eds.), *Quality and Reliability of Large-Eddy Simulations*, ERCOFTAC Series, vol. 12, Springer, 2008.
- [19] A. Leonard, Energy cascade in large eddy simulations of turbulent fluid flows, *Adv. Geophys. A* 18 (1974) 237–248.
- [20] S. Ghosal, An analysis of numerical errors in Large Eddy Simulations of turbulence, *J. Comput. Phys.* 125 (1996).
- [21] I. Fedjoun, N. Lardjane, I. Gokalp, Revisiting numerical errors in direct and large eddy simulations of turbulence: physical and spectral spaces analysis, *J. Comput. Phys.* 174 (2001) 816–851.
- [22] F.K. Chow, P. Moin, A further study of numerical errors in large-eddy simulations, *J. Comput. Phys.* 184 (2003) 366–380.
- [23] N. Park, J.Y. Yoo, H. Choi, Discretization errors in large eddy simulation: on the suitability of centered and upwind-biased compact difference schemes, *J. Comput. Phys.* 198 (2004) 580–616.
- [24] B.J. Geurts, F. van der Bos, Numerically induced high-pass dynamics in large-eddy simulation, *Phys. Fluids* 17 (2005) 125103.
- [25] J.C. Magnien, P. Sagaut, M. Deville, A study of built-in filter for some eddy viscosity models in large-eddy simulation, *Phys. Fluids* 13 (2001) 5.
- [26] F.M. Denaro, A 3D second-order accurate projection-based Finite Volume code on non-staggered, non-uniform structured grids with continuity preserving properties: application to buoyancy-driven flows, *Int. J. Numer. Methods Fluids* 52 (4) (2006) 393–432.
- [27] G. De Stefano, O.V. Vasilyev, Sharp cut-off versus smooth filtering in large eddy simulation, *Phys. Fluids* 14 (2002) 1.
- [28] A.G. Kravchenko, P. Moin, On the effect of numerical errors in Large Eddy Simulations of turbulent flows, *J. Comput. Phys.* 131 (1997).
- [29] C.D. Pruett, T.B. Gatski, C.E. Grosch, W.D. Thacker, The temporally filtered Navier–Stokes equations: properties of the residual stress, *Phys. Fluids* 15 (2003) 8.
- [30] N.A. Adams, S. Hickel, S. Franz, Implicit subgrid-scale modeling by adaptive deconvolution, *J. Comput. Phys.* 200 (2004) 412–431.
- [31] F.M. Denaro, Time-accurate intermediate boundary conditions for large eddy simulations based on projection methods, *Int. J. Numer. Methods Fluids* 48 (2005).
- [32] S. Leonard, M. Terracol, P. Sagaut, Commutation error in LES with time-dependent filter width, *Comput. Fluids* 36 (2007) 513–519.
- [33] C.D. Pruett, Temporal large-eddy simulation: theory and implementation, *Theor. Comput. Fluid Dyn.* 22 (2008) 275–304.
- [34] A. Arovitola, F.M. Denaro, On the application of congruent upwind discretizations for large eddy simulations, *J. Comput. Phys.* 194 (1) (2004) 329–343.
- [35] F.M. Denaro, Towards a new model-free simulation of high Reynolds flows: local average direct numerical simulation, *Int. J. Numer. Methods Fluids* 23 (1996) 125–142.
- [36] G. Riccardi, Private Communication, 2009.
- [37] C. Canuto, M.Y. Hussaini, A. Quarteroni, T.A. Zang, *Spectral Methods. Evolution to Complex Geometries and Applications to Fluid Dynamics*, Springer, 2007.
- [38] V. Levasseur, P. Sagaut, M. Mallet, Subgrid models for large-eddy simulation using unstructured grids in a stabilized finite element framework, *J. Turbulence* 7 (2006) 28.
- [39] F.F. Grinstein, L.G. Margolin, W.J. Rider (Eds.), *Implicit Large Eddy Simulation*, Cambridge, 2007.
- [40] R.W.C.P. Verstappen, A.E.P. Veldman, Symmetry-preserving discretisation of turbulent flow, *J. Comput. Phys.* 187 (2003) 343–368.
- [41] O. Zikanov, S.N. Slinn, M.R. Dhanak, Turbulent convection driven by surface cooling in shallow water, *J. Fluid Mech.* 464 (2002).
- [42] F.M. Denaro, G. De Stefano, A new development of the dynamic procedure in large-eddy simulation based on a Finite Volume integral approach, Application to stratified turbulence, *Theor. Comp. Fluid Dyn.*, 2010. Online: doi:10.1007/s00162-010-0202-x.
- [43] J. Meyers, B.J. Geurts, M. Baelmans, Database analysis of errors in large-eddy simulation, *Phys. Fluids* 15 (9) (2003) 2740–2755.
- [44] F. Sarghini, U. Piomelli, E. Balaras, Scale-similar model for large-eddy simulations, *Phys. Fluids* 11 (6) (1999) 1596–1607.
- [45] S.B. Pope, Ten questions concerning the large-eddy simulation of turbulent flows, *New J. Phys.*, 6 (2004) 35. Online at: <http://www.njp.org/>.
- [46] R.D. Moser, J. Kim, N.N. Mansour, Direct numerical simulation of turbulent channel flow up to $Re_\tau = 590$, *Phys. Fluids* 11 (1999) 4.
- [47] S. Stolz, N.A. Adams, L. Kleiser, An approximate deconvolution model for large-eddy simulation with application to incompressible wall-bounded flows, *Phys. Fluids* 13 (2001) 4.
- [48] V.C. Wong, D.K. Lilly, A comparison of two dynamic subgrid closure methods for turbulent thermal convection, *Phys. Fluids* 6 (5) (1994).
- [49] F. van der Bos, B.J. Geurts, Computational error-analysis of a discontinuous Galerkin discretization applied to large-eddy simulation of homogeneous turbulence, *Comput. Methods Appl. Mech. Eng.* 199 (2010) 903–915.
- [50] J. Meyers, P. Sagaut, Is plane-channel flow a friendly case for the testing of large-eddy simulation subgrid-scale models?, *Phys. Fluids* 19 (2007) 048105.
- [51] S.T. Bose, P. Moin, D. You, Grid-independent large-eddy simulation using explicit filtering, *Phys. Fluids* 22 (2010) 105103.